Chapter 1

Recrystallization Textures of Metals and Alloys

Dong Nyung Lee and Heung Nam Han

Additional information is available at the end of the chapter

http://dx.doi.org/10.5772/54123

1. Introduction

Recrystallization (Rex) takes place through nucleation and growth. Nucleation during Rex can be defined as the formation of strain-free crystals, in a high energy matrix, that are able to grow under energy release by a movement of high-angle grain boundaries. The nucleus is in a thermodynamic equilibrium between energy released by the growth of the nucleus (given by the energy difference between deformed and recrystallized volume) and energy consumed by the increase in high angle grain boundary area. This means that a critical nucleus size or a critical grain boundary curvature exists, from which the newly formed crystal grows under energy release. This definition is so broad and obscure that crystallization of amorphous materials is called Rex by some people, and Rex can be confused with the abnormal grain growth when grains with minor texture components can grow at the expense of neighboring grains with main texture components because the minor-component grains can be taken as nuclei. Here we will present a theory which can determine whether grains survived during deformation act as nuclei and which orientation the deformed matrix is destined to assume after Rex. A lot of Rex textures will be explained by the theory.

2. Theories for evolution of recrystallization textures

Rex occurs by nucleation and growth. Therefore, the evolution of the Rex texture must be controlled by nucleation and growth. In the oriented nucleation theory (ON), the preferred activation of a special nucleus determines the final Rex texture [1]. In the oriented growth theory (OG), the only grains having a special relationship to the deformed matrix can preferably grow [2]. Recent computer simulation studies tend to advocate ON theory [3]. This comes from the presumption that the growth of nuclei is predominated by a difference in

energy between the nucleus and the matrix, or the driving force. In addition to this, the weakness of the conventional OG theory is in much reliance on the grain boundary mobility.

One of the present authors (Lee) advanced a theory for the evolution of Rex textures [4] and elaborated later [5,6]. In the theory, the Rex texture is determined such that the absolute maximum stress direction (AMSD) due to dislocation array formed during fabrication and subsequent recovery is parallel to the minimum Young's modulus direction (MYMD) in recrystallized (Rexed) grains and other conditions are met, whereby the strain energy release can be maximized. In the strain-energy-release-maximization theory (SERM), elastic anisotropy is importantly taken into account.

In what follows, SERM is briefly described. Rex occurs to reduce the energy stored during fabrication by a nucleation and growth process. The stored energy may include energies due to vacancies, dislocations, grain boundaries, surface, etc. The energy is not directional, but the texture is directional. No matter how high the energy may be, the defects cannot directly be related to the Rex texture, unless they give rise to some anisotropic characteristics. An effect of anisotropy of free surface energy due to differences in lattice surface energies can be neglected except in the case where the grain size is larger than the specimen thickness in vacuum or an inert atmosphere. Differences in the mobility and/or energy of grain boundaries must be important factors to consider in the texture change during grain growth. Vacancies do not seem to have an important effect on the Rex texture due to their relatively isotropic characteristics. The most important driving force for Rex (nucleation and growth) is known to be the stored energy due to dislocations. The dislocation density may be different from grain to grain. Even in a grain the dislocation density is not homogeneous. Grains with low dislocation densities can grow at the expanse of grains with high dislocation densities. This may be true for slightly deformed metals as in case of strain annealing. However, the differences in dislocation density and orientation between grains decrease with increasing deformation. Considering the fact that strong deformation textures give rise to strong Rex textures, the dislocation density difference cannot be a dominant factor for the evolution of Rex textures. Dislocations cannot be related to the Rex texture, unless they give rise to anisotropic characteristics.

The dislocation array in fabricated materials looks very complicated. Dislocations generated during plastic deformation, deposition, etc., can be of edge, screw, and mixed types. Their Burgers vectors can be determined by deformation mode and texture, and their array can be approximated by a stable or low energy arrangement of edge dislocations after recovery. Figure 1 shows a schematic dislocation array after recovery and principal stress distributions around stable and low energy configurations of edge dislocations, which were calculated using superposition of the stress fields around isolated dislocations, or, more specifically, were obtained by a summation of the components of stress field of the individual dislocations sited in the array. It can be seen that AMSD is along the Burgers vector of dislocations that are responsible for the long-range stress field. The volume of crystal changes little after heavy deformation because contraction in the compressive field and expansion in the tensile fields around dislocations generated during deformation compensate each other. That is, this process takes place in a displacement controlled system. The uniaxial specimen in Figure 2 makes an example of the displace-

ment controlled system. When a stress-free specimen S_0 is elastically elongated by ΔL by force F_A (Figure 2a), the elongated specimen S_F has an elastic strain energy represented by triangle *OAC* (Figure 2b). When V in S_F is replaced by a stress-free volume V, S_R having the stress free V has the strain energy of *OBC* (Figure 2b.) Transformation from the S_F state to the S_R state results in a strain-energy-release represented by *OAB* (Figure 2b). The strain-energy-release can be maximized when the S_F and S_R states have the maximum and minimum strain energies, respectively. In this case, AMSD is the axial direction of S_F, and the S_R state has the minimum energy when MYMD of the stress-free V is along the axial direction that is AMSD. In summary, the strain energy release is maximized when AMSD in the high dislocation density matrix is along MYMD of the stress free crystal, or nucleus. That is, when a volume of *V* in the stress field is replaced by a stress-free single crystal of the volume *V*, the strain energy release of the system occurs. The strain energy release can change depending on the orientation of the stress-free crystal. The strain energy release is maximized when AMSD in the high energy matrix is along MYMD of the stress-free crystal. The stress-free grains formed in the early stage are referred to as nuclei, if they can grow. The orientation of a nucleus is determined such that its strain energy release per unit volume during Rex becomes maximized.

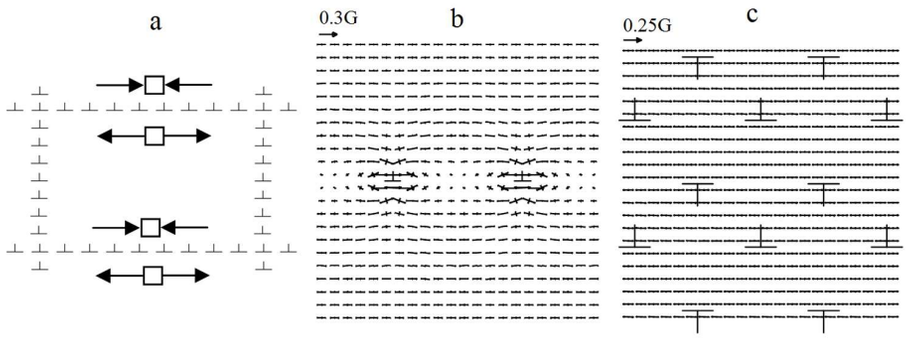

Figure 1. (a) Schematic dislocation array after recovery, where horizontal arrays give rise to long-range stress field, and vertical arrays give rise to short-range stress field [7]. Principal stress distributions around parallel edge dislocations calculated based on (b) 100 linearly arrayed dislocations with dislocation spacing of 10**b**, and (c) low energy array of 100 x 100 dislocations. **b** is Burgers vector and G is shear modulus [8].

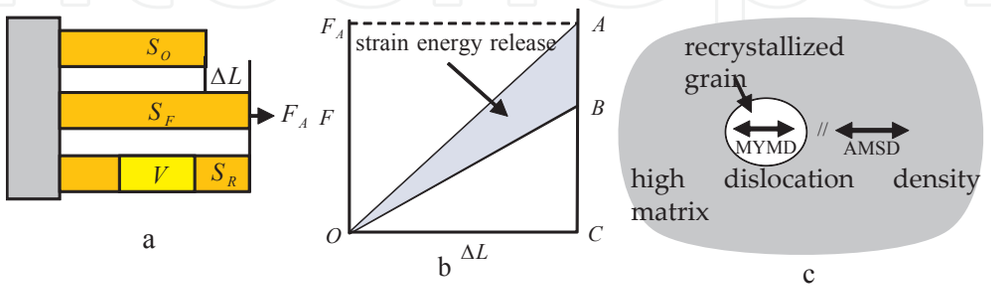

Figure 2. Displacement controlled uniaxial specimen for explaining strain-energy-release being maximized when AMSD in high dislocation density matrix is along MYMD in recrystallized grain.

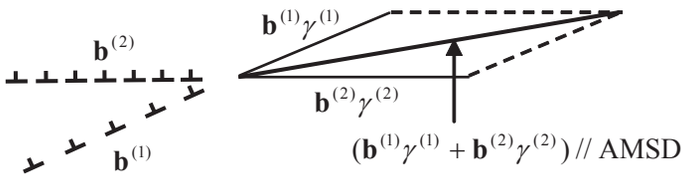

Figure 3. AMSD for active slip systems *i* whose Burgers vectors are $\mathbf{b}^{(i)}$ and activities are $\gamma^{(i)}$.

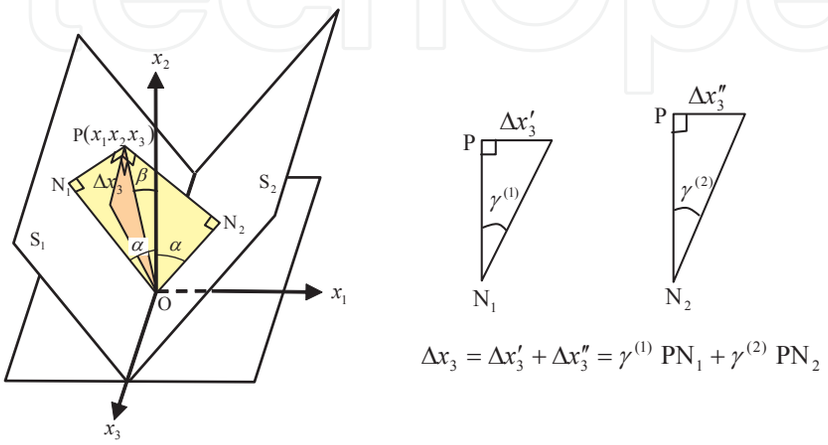

Figure 4. Schematic of two slip planes S_1 and S_2 that share common slip direction along x_3 axis.

We first calculate AMSD in an fcc crystal deformed by a duplex slip of (111)[-101] and (111)[-110] that are equally active. The duplex slip can be taken as a single slip of (111)[-211], which is obtained by the sum of the two slip directions. In this case, the maximum stress direction is [-211]. However, some complication can occur. One slip system has two opposite directions. The maximum stress direction for the (111)[-101] slip system represents the [-101] direction and its opposite direction, [1 0-1]. The maximum stress direction for the (111)[-110] slip system represents the [-110] and [1-1 0] directions. Therefore, there are four possible combinations to calculate the maximum stress direction, [-101] + [-110] = [-211], [-101] + [1-1 0] = [0-1 1], [1 0-1] + [-110] = [0 1-1], and [1 0-1] + [1-1 0] = [2-1-1], among which [-211]//[2-1-1] and [0-1 1]//[0 1-1]. The correct combinations are such that two directions make an acute angle. If the two slip systems are not equally active, the activity of each slip system should be taken into account. If the (111)[-101] slip system is two times more active than the (111)[-110] system, the maximum stress direction becomes 2[-101] + [-110] = [-312]. This can be generalized to multiple slip. For multiple slip, AMSD is calculated by the sum of active slip directions of the same sense and their activities, as shown in Figure 3. It is convenient to choose slip directions so that they can be at acute angles with the highest strain direction of the specimen, e.g., RD in rolled sheets, the axial direction in drawn wires, etc.

When two slip systems share the same slip direction, their contributions to AMSD are reduced by 0.5 for bcc metals and 0.577 for fcc metals as follows. Figure 4 shows two slip planes, S_1 and S_2, intersecting along the common slip direction, the x_3 axis; the x_2 axis bisects the angle between the poles of these planes. The loading direction lies within the quadrant drawn between S_1 and

S_2, and the displacement Δx_3 along the x_3 axis at any point P with coordinates (x_1,x_2,x_3) is considered. If shear strains $\gamma^{(1)}$ and $\gamma^{(2)}$ occur on the slip system 1 (the slip plane S_1 and the slip direction x_3) and the slip system 2 (the slip plane S_2 and the slip direction x_3), respectively, then

$$\Delta x_3 = \gamma^{(1)}\ \mathrm{PN}_1 + \gamma^{(2)}\ \mathrm{PN}_2 \tag{1}$$

where PN_1 and PN_2 are normal to the planes S_1 and S_2, respectively. Therefore,

$$\mathrm{PN}_1 = \mathrm{OP}\sin(\alpha - \beta) \text{and}\ \ \mathrm{PN}_2 = \mathrm{OP}\sin(\alpha + \beta) \tag{2}$$

where OP, α, and β are defined in Figure 4. Therefore,

$$\Delta x_3 = (\gamma^{(1)} + \gamma^{(2)})\ \mathrm{OP}\sin\alpha\cos\beta + (\gamma^{(2)} - \gamma^{(1)})\ \mathrm{OP}\cos\alpha\sin\beta \tag{3}$$

Because $\alpha > \beta$ and $(\gamma^{(1)} + \gamma^{(2)}) > (\gamma^{(2)} - \gamma^{(1)})$, the second term of the right hand side is negligible compared with the first term. It follows from $\mathrm{OP}\cos\beta = x_2$ that $\Delta x_3 \approx (\gamma^{(1)} + \gamma^{(2)})\, x_2 \sin\alpha$. Therefore, the displacement Δx_3 is linear with the x_2 coordinate, and the deformation is equivalent to single slip in the x_3 direction on the $(\gamma^{(1)}S_1 + \gamma^{(2)}S_2)$ plane. The apparent shear strain γ_a is

$$\gamma_a = \Delta x_3 / x_2 \approx (\gamma^{(1)} + \gamma^{(2)})\ \sin\alpha \tag{4}$$

The apparent shear strains $\gamma_a^{(i)}$ on the slip systems i are

$$\gamma_a^{(i)} = \gamma^{(i)}\sin\alpha \tag{5}$$

For bcc metals, $\sin\alpha = 0.5$ (e.g. a duplex slip of (101)[1 1-1] and (011)[1 1-1]) and hence

$$\gamma_a^{(i)}\left(\mathrm{bcc}\right) = 0.5\gamma^{(i)} \tag{6}$$

For fcc metals, $\sin\alpha = 0.577$ (e.g. a duplex slip of (-1 1-1)[110] and (1-1-1)[110]) and hence

$$\gamma_a^{(i)}\left(\mathrm{fcc}\right) = 0.577\gamma^{(i)} \tag{7}$$

The activity of each slip direction is linearly proportional to the dislocation density ρ on the corresponding slip system, which is roughly proportional to the shear strain on the slip system. Experimental results on the relation between shear strain γ and ρ are available for Cu and Al [9].

If a crystal is plastically deformed by $\delta\varepsilon$ (often about 0.01), then we can calculate active slip systems i and shear strains $\gamma^{(i)}$ on them using a crystal plasticity model, resulting in the shear strain rate with respect to strain of specimen, $d\gamma^{(i)}/d\varepsilon$. During this deformation, the crystal can rotate, and active slip systems and shear strains on them change during $\delta\varepsilon$. When a crystal

rotates during deformation, the absolute value of shear strain rates $|d\gamma^{(i)}/d\varepsilon|$ on slip systems i can vary with strain ε of specimen. For a strain up to $\varepsilon = e$, the contribution of each slip system to AMSD is proportional to

$$\gamma^{(i)} = \int_0^e \left| d\gamma^{(i)} / d\varepsilon \right| d\varepsilon \tag{8}$$

The above equation is illustrated in Figure 5. If a deformation texture is stable, the shear strain rates on the slip systems are independent of deformation.

So far methods of obtaining AMSD have been discussed. This is good enough for prediction of fiber textures. However, the stress states around dislocation arrays are not uniaxial but triaxial. Unfortunately we do not know the stress fields of individual dislocations in real crystals, but know Burgers vectors. Therefore, AMSD obtained above applies to real crystals. Any stress state has three principal stresses and hence three principal stress directions which are perpendicular to each other. Once we know the three principal stress directions, the Rex textures are determined such that the three directions in the deformed matrix are parallel to three <100> directions in the Rexed grain, when MYMDs are <100>. In figure 6, let the unit vectors of **A**, **B**, and **C** be ***a*** [a_1 a_2 a_3], ***b*** [b_1 b_2 b_3], and ***c*** [c_1 c_2 c_3], where a_i are direction cosines of the unit vector ***a*** referred to the crystal coordinate system. AMSD is one of three principal stress directions. Two other principal stresses are obtained as explained in Figure 6.

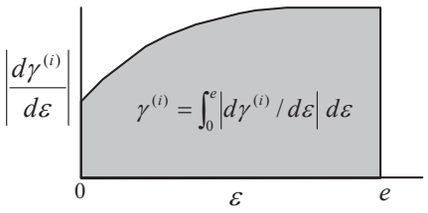

Figure 5. Calculation of $\gamma^{(i)}$ for crystal rotation during deformation up to $\varepsilon = e$.

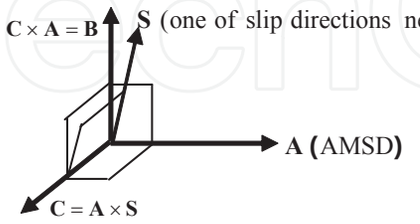

Figure 6. Relationship between three principal stress directions **A**, **B**, and **C**.

If the unit vectors ***a***, ***b***, and ***c*** are set to be along [100], [010], and [001] after Rex, components of the unit vectors are direction cosines relating the deformed and Rexed crystal coordinate systems, when MYMDs are <100>. That is, the $(hkl)[uvw]$ deformation orientation is calculated to transform to the $(h_r\ k_r\ l_r)[u_r\ v_r\ w_r]$ Rex orientation using the following equation.

$$\begin{pmatrix} h_r \\ k_r \\ l_r \end{pmatrix} = \begin{pmatrix} a_1 & a_2 & a_3 \\ b_1 & b_2 & b_3 \\ c_1 & c_2 & c_3 \end{pmatrix} \begin{pmatrix} h \\ k \\ l \end{pmatrix} \quad \begin{pmatrix} u_r \\ v_r \\ w_r \end{pmatrix} = \begin{pmatrix} a_1 & a_2 & a_3 \\ b_1 & b_2 & b_3 \\ c_1 & c_2 & c_3 \end{pmatrix} \begin{pmatrix} u \\ v \\ w \end{pmatrix} \tag{9}$$

It should be mentioned that ***a*** is set to be along [100], but ***b*** is along [010] or [001] depending on physical situations and c is consequently along [001] or [010]. The Rex texture can often be obtained without resorting to the above process because the AMSD//MYMD condition is so dominant that the Rex texture can be obtained by the following priority order.

The 1st priority: When AMSD is cristallographically the same as MYMD, No texture changes after Rex [10].

The 2nd priority: When AMSD crystallographically differs from MYMD, the Rex texture is determined such that AMSD in the matrix is parallel to MYMD in the Rexed grain, with one common axis of rotation between the deformed and Rexed states. The common axis can be ND, TD, or other direction (e.g. <110> for bcc metals). This may be related to minimum atomic movement at the AMSD//MYMD constraints. However, we do not know the exact physical picture of this.

The 3rd priority: When the first two conditions are not met, the method explained to obtain Eq. 9 is used.

3. Electrodeposits and vapor-deposits

When the density of dislocations in electrodeposits and vapor deposits is high, the deposits undergo Rex when annealed. AMSD in the deposits can be determined by their textures. The density of dislocations whose Burgers vectors are directed away from the growth direction (GD)of deposits was supposed to be higher than when the Burgers vector is nearly parallel to GD because dislocations whose Burgers vector is close to GD are easy to glide out from the deposits by the image force during their growth [11]. This was experimentally proved in a Cu electrodeposit with the <111> orientation [12]. Therefore, AMSDs are along the Burgers vectors nearly normal to GD.

3.1. Copper, nickel, and silver electrodeposits

Lee et al. found that the <100>, <111>, and <110> textures (inverse pole figures: IPFs) of Cu electrodeposits which were obtained from Cu sulfate and Cu fluoborate baths [13,14], and a cyanide bath [15] changed to the <100>, <100>, and <√310> textures, respectively, after Rex as shown in Figure 7. The texture fraction (TF) of the (*hkl*) reflection plane is defined as follows:

$$\mathrm{TF}(hkl) = \frac{\mathrm{I}(hkl)/\mathrm{I}_{\mathrm{o}}(hkl)}{\sum\left[\mathrm{I}(hkl)/\mathrm{I}_{\mathrm{o}}(hkl)\right]} \tag{10}$$

where I(*hkl*) and I_o(*hkl*) are the integrated intensities of (*hkl*) reflections measured by x-ray diffraction for an experimental specimen and a standard powder sample, respectively, and Σ means the summation. When TF of any (*hkl*) plane is larger than the mean value of TFs, a preferred orientation or a texture exists in which grains are oriented with their (*hkl*) planes parallel to the surface, or with their <*hkl*> directions normal to the surface. When TFs of all reflections are the same, the distribution of crystal orientation is random. TFs of all the reflections sum up to unity. Figure 7 indicates that the deposition texture of <100> remains unchanged after Rex. This is expressed as $<100>_D \rightarrow <100>_R$. All the samples were freestanding and so subjected to no external external stresses during annnealing. The results are explained by SERM in Section 2. We have to know MYMD of Cu and AMSDs of Cu electrodeposits. Young's modulus *E* of cubic crystals can be calculated using Eq. 11 [16].

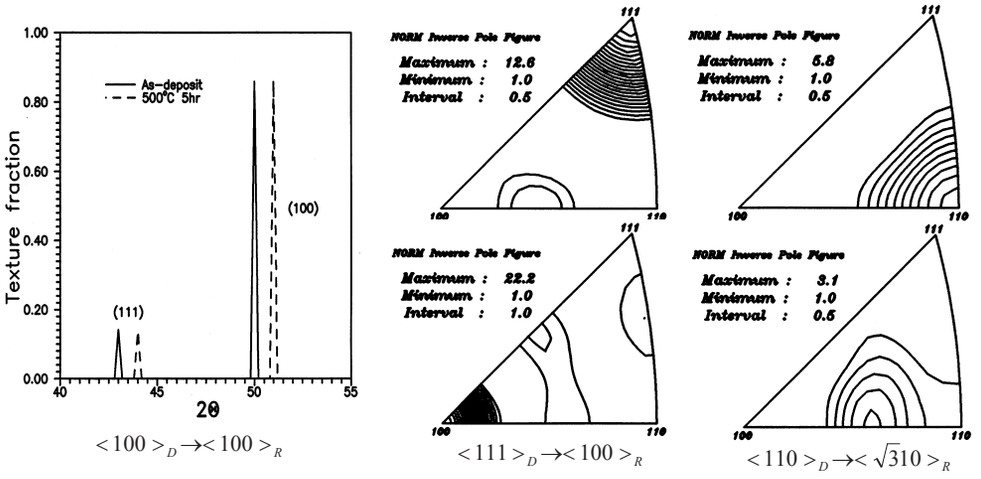

Figure 7. Deposition and Rex textures of Cu electrodeposits. $<hkl>_D \rightarrow <uvw>_R$ means that <*hkl*> deposition texture changes to <*uvw*> Rex texture. For $<100>_D$, Rex peaks are shifted rightward by 1º from their original positions to be distinguished from deposition peaks. TF data [13] and IPFs [14].

$$1/E = S_{11} + [S_{44} - 2(S_{11} - S_{12})](a_{11}^2 a_{12}^2 + a_{12}^2 a_{13}^2 + a_{13}^2 a_{11}^2) \tag{11}$$

where S_{ij} are compliances and a_{1i} are the direction cosines relating the uniaxial stress direction x'_1 to the symmetry axes x_i. When $[S_{44}\text{-}2(S_{11}\text{-}S_{12})] < 0$, or $A=2(S_{11}\text{-}S_{12})/S_{44} > 1$, $(a_{11}^2 a_{12}^2 + a_{12}^2 a_{13}^2 + a_{13}^2 a_{11}^2) = 0$ yields the minimum Young's modulus, which is obtained at $a_{11} = a_{12} = a_{13} = 0$. Therefore, MYMDs are parallel to <100>. When $[S_{44}\text{-}2(S_{11}\text{-}S_{12})]>0$, or $A< 1$, the maximum value of $(a_{11}^2 a_{12}^2 + a_{12}^2 a_{13}^2 + a_{13}^2 a_{11}^2)$ yields the minimum Young's modulus, which is obtained at $a_{11}^2 = a_{12}^2 = a_{13}^2 = 1/3$. Therefore, MYMDs are parallel to <111>. When $[S_{44}\text{-}2(S_{11}\text{-}S_{12})] = 0$, or $A = 1$, *E* is independent of direction, in other words, the elastic properties are isotropic. *A* is usually referred to as Zener's anisotropy factor. Summarizing, MYMDs // <100> for $A>1$, MYMDs// <111> for $A<1$, and elastic isotropy for $A=1$.

For fcc Cu, S_{11}=0.018908, S_{44} =0.016051, S_{12} = -0.008119 GPa^{-1} at 800 K [17], which in turn gives rise to $[S_{44}-2(S_{11}-S_{12})] < 0$, and so MYMDs are <100>. MYMDs and the Burgers vectors of Cu are along the <100> directions and the <110> directions, respectively. There are six equivalent directions in the <110> directions, with opposite directions being taken as the same. As already explained, AMSD is along the Burgers vector which is approximately normal to GD.

For the <100> oriented Cu (simply <100> Cu) deposit, two of the six <110> directions are at 90° and the remaining four are at 45° with GD, as shown in Figure 8. The two <110> directions, which is AMSD, change to the <100> directions after Rex, resulting in the <100> Rex texture (Figure 8b) in agreement with the experimental result.

For the <111> Cu deposit, three of the six <110> directions are at right angles with the [111] GD; the remaining three <110> directions are at 35.26° with GD, as shown in Figure 9 a. The former three <110> directions, AMSD, can change to <100> after Rex, but angles between the <110> directions are 60° and the angle between the <100> directions is 90°. Correspondence between the <110> directions in as-deposited grains and the <100> directions in Rexed grains is therefore impossible in a grain. Two of the <110> directions in neighboring grains, which are at right angles with each other, can change to the <100> directions to form the <100> nuclei in grain boundaries, which grow at the expense of high energy region, as shown in Figure 9b. Thus, the <111> deposition texture change to the <100> Rex texture, in agreement with the measured result.

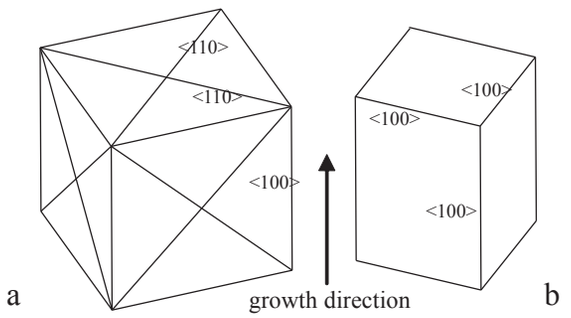

Figure 8. Drawings explaining that <100> deposition texture (a) remains unchanged after Rex (b).

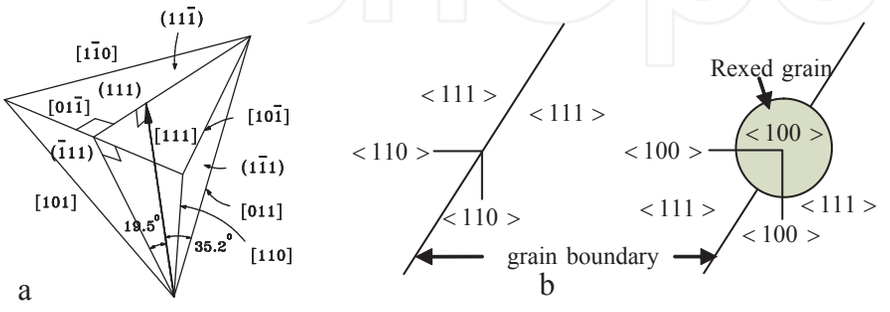

Figure 9. (a) <110> directions in <111> oriented fcc crystal in which arrow indicates [111] growth direction. (b) Drawings for explanation of <111> deposition to <100> Rex texture transformation.

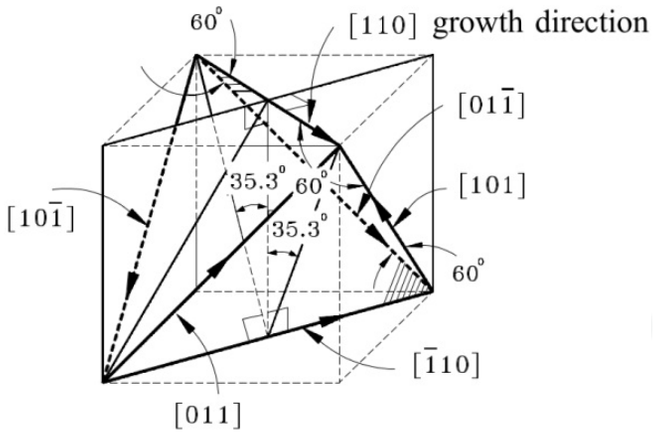

Figure 10. directions in [110] oriented fcc crystal.

For the <110> Cu deposit, one <110> direction is normal to the <110> GD and the remaining four <110> directions are at 60° with the <110> GD, as shown in Figure 10. The first one of the <110> directions and the last four <110> directions are likely to determine the Rex texture because the last four directions are closer to the deposit surface than to GD. Recalling that the <110> directions change to <100> directions after Rex, GD of Rexed grains should be at 60° and 90° with the <100> directions, MYMD, at the same time. GD satisfying the condition is <√310>, in agreement with the experimental results.

So far we have discussed the evolution of the Rex textures from simple deposition textures. A Cu deposit whose texture can be be approximated by a weak duplex texture consisting of the <111> and <110> orientations developed the Rex texture which is approximated by a weak <√310> orientation rather than <100> + <√310> [18]. For the duplex deposition texture, the Rex texture may not consist of the Rex orientation components from the deposition orientation components because differently oriented grains can have different energies. The tensile strengths of copper electrodeposits showed that the tensile strength of the specimens with the <110> texture was higher than those with the <111> texture obtained from the similar electrodeposition condition. This implies that the <110> specimen has the higher defect densities than the <111> specimen [18,19]. Therefore, the <110> grains are likely to have higher driving force for Rex than the <111> grains, resulting in the <√310> texture after Rex, in agreement with experimental result [18].

For Ni, S_{11}= 0.009327, S_{44} = 0.009452, S_{12} = -0.003694 GPa^{-1} at 760 K [20], which in turn gives rise to $[S_{44}\text{-}2(S_{11}\text{-}S_{12})] < 0$, and so MYMDs are <100>. Therefore, the deposition to Rex texture transformation of Ni electrodeposits is expected to be similar to that of Cu electrodeposits. As expected, freestanding Ni electrodeposits of 30-50 μm in thickness showed that the <100> deposition texture remained unchanged after Rex, and the <110> deposition texture changed to <√310> after Rex [21].

For Ag, S_{11}= 0.03018, S_{44} = 0.02639, S_{12} = -0.0133 GPa^{-1} at 750 K [17], which in turn gives $[S_{44}\text{-}2(S_{11}\text{-}S_{12})] < 0$, and so MYMDs are <100>. Therefore, the deposition to Rex texture transformation of freestanding Ag electrodeposits is expected to be similar to that of Cu electrode-

posits. Figure 11 shows four different deposition and corresponding Rex textures of Ag electrodeposits. Samples a, b, and c shows results similar to Cu electrodeposits, except that minor <221> component, which is the primary twin component of the <100> component in the Rex textures, is stronger than that of Cu deposits. The strong development of twins in Ag is due to its lower stacking fault energy (~22 mJm^{-2}) than that of Cu (~80 mJm^{-2}).

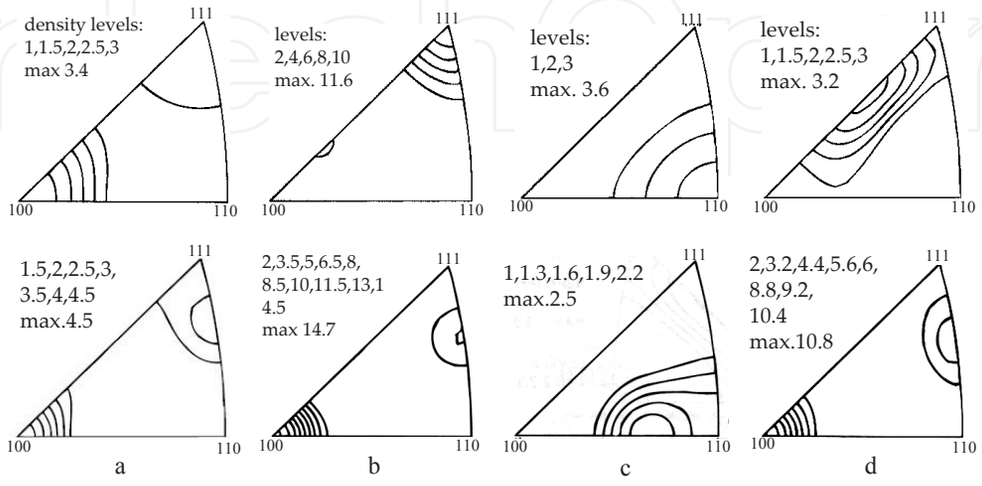

Figure 11. Deposition (top) and Rex (bottom) textures (IPFs) of Ag electrodeposits [22].

The deposition texture of Sample d was well described by 0.32<112> + 0.14$<127>_T$ + 0.25<113> + 0.23$<557>_T$ + 0.06$<19\ 19\ 13>_{TT}$ with each of individual orientations being superimposed with a Gaussian peak of 8°. Here $<127>_T$ indicates the twin orientation of its preceeding <112> orientation, and TT indicates secondary twin. Thus, the main components in deposition texture of Sample d are <112>, <113>, and <557>. The <110> directions that are nearly normal to GD will be AMSD and in turn determine the Rex texture. Table 1 gives angles between <110> and [11w]. Table 1 shows that the probability of <110> directions being normal to GD is the highest. The <110> directions normal to GD will become parallel to the <100> directions (MYMS) after Rex. Therefore, the Rex texture will be the <100> orientation for the same reason as in the <111> orientation of the deposit [22].

3.2. Chromium electrodeposits

Table 2 shows TFs (Eq. 10) of Cr electrodeposits obtained under three electrodeposition conditions. Specimen Cr-A has a strong <111> fiber texture. The texture of Cr-B is characterized by weak <111>, and that of Cr-C is by weak <100>. The optical microstructure and hardness test results and others indicated that all the specimens were fully Rexed at 1173 K. TFs as functions of annealing temperature and time in Figure 12 indicate that the deposition texture of Cr-A little change after Rex. The pole figures in Figures 13 and 14 indicate the deposition textures of Cr-B and Cr-C little change after Rex. In conclusion, the <100> and <111> deposition textures of Cr electrodeposits little change after Rex. These results are compatible with SERM as discussed in what follows. There are four equivalent <111> directions in bcc Cr crystal, with opposite directions being taken as the same. For the <111> Cr deposit, one of four <111>

directions is along GD and the remaining three <111> directions are at an angle of 70.5° with GD (Figure 15). The remaining three <111> directions can be AMSDs. They will become parallel to MYMDs of Rexed grains. The compliances of Cr are S_{11} =0.00314, S_{44} = 0.0101, S_{12} = -0.000567 GP^{-1} at 500 K [23], which lead to $[S_{44}-2(S_{11}-S_{12})] > 0$. Therefore, MYMDs of Cr are <111>, which are also AMSDs of the deposit. Therefore, the <111> and <100> textures of Cr deposits do not change after Rex, as can be seen from Figure 15, in agreement with experimental results.

	110	**-110**	**101**	**-101**	**011**	**0-1 1**
557	44.7	90	31.5	81.8	31.5	81.8
112	54.7	90	30	73.2	30	73.2
113	64.8	90	31.5	64.8	31.5	64.8

Table 1. Angles between <110> and [11w] directions (°)

	(110)	**(200)**	**(211)**	**(220)**	**(310)**	**(222)**	**Texture**
Cr-A	0.02	0.05	0	0	0	**0.93**	Strong <111>
Cr-B	0.03	0.15	0.28	0	0.01	**0.53**	<111>
Cr-C	0.19	**0.47**	0.13	0.05	0.13	0.03	<100>

Table 2. Texture fractions (TF) of reflection planes of Cr electrodeposits A, B, and C [14]. Bold-faced numbers indicate highest TFs in corresponding deposits.

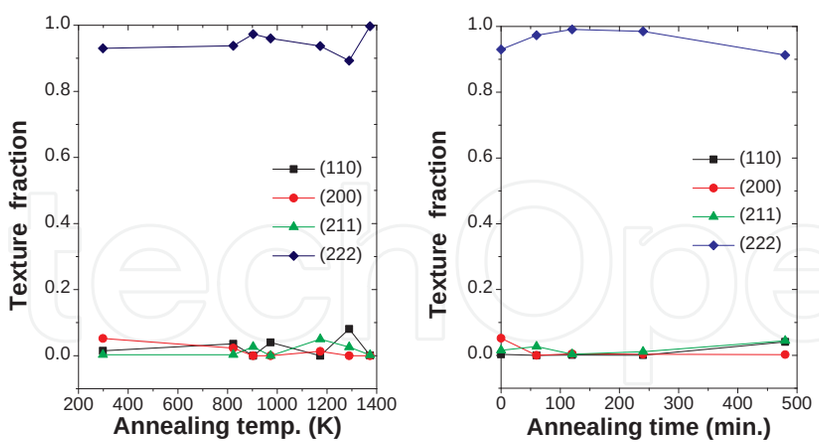

Figure 12. TFs of Cr-A as functions of annealing (a) temperature for 1 h and (b) time at 903 K [14].

3.3. Copper and silver vapor-deposits

Patten et al. [24] formed deposits of Cu up to 1mm in thickness at room temperature in a triode sputtering apparatus using a krypton discharge under various conditions of sputtering rate,

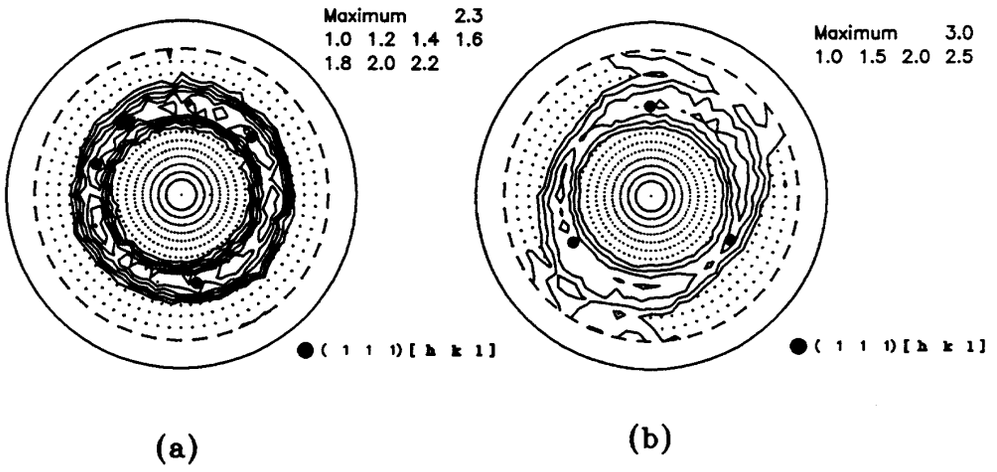

Figure 13. (200) pole figures of Cr-B (left) before and (right) after annealing at 1173 K for 1 h [14].

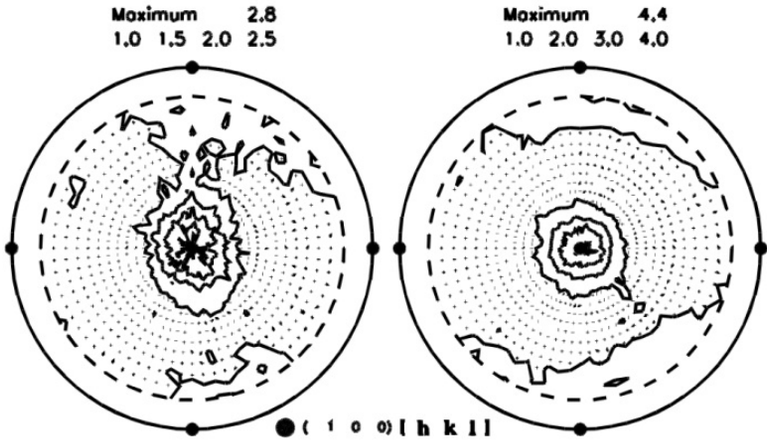

Figure 14. (200) pole figures of Cr-C (left) before and (right) after annealing at 1173 K for 1 h [14].

gas purity, and substrate bias. The 3.81 cm diameter target was made from commercial grade OFHC forged Cu-bar stock containing approximately 100 ppm oxygen by weight with only traces of other elements. The substrates were 2.54 cm diameter by 6.2 mm thick disks made of OFHC Cu. These disks were electron beam welded to a stainless-steel tube to provide direct water-cooling for temperature control during sputtering. As-deposited grains were approximately 100 nm in diameter. Room-temperature Rex and grain growth displaying no twins were observed approximately 9 h after removal from the sputtering apparatus. Nucleation sites were almost randomly distributed. Hardness of the unrecrystallized matrix remained at ~230 DPH from the time it was sputtered until Rex, when it abruptly dropped to approximately 60 DPH in the Rexed grains. Rex resulted in a texture transformation from the <111> deposition texture to the <100> Rex texture. Since the substrate is also Cu, the orientation transition from <111> to <100> cannot be attributed to thermal strains. The driving force for Rex must be the

internal stress due to defects such as vacancies and dislocations. Therefore, the texture transition is consistent with the prediction of SERM.

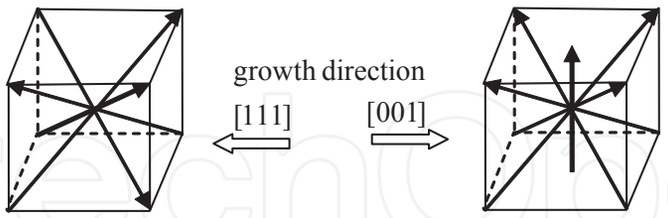

Figure 15. Thin arrows (AMSDs) and thick arrows (GD) in [111] and [001] Cr crystals.

Greiser et al. [25] measured the microstructure and texture of Ag thin films deposited on different substrates using DC magnetron sputtering under high vacuum conditions (base pressure: 10^{-8} mbar, partial Ar pressure during deposition: 10^{-3} mbar). A weak <111> texture in a 0.6 μm thick Ag film deposited on a (001) Si wafer with a 50 nm thermal SiO_2 layer at room temperature becomes stronger with increasing thickness. It is generally accepted that a random polycrystalline structure is obtained up to a critical film thickness unless an epitaxial growth condition is satisfied. Therefore, the <111> texture developed in the 0.6 μm film was weak and became stronger with increasing thickness. This is consistent with the preferred growth model [26]. They also found that the texture of the film deposited at room temperature was "high <111>", whereas the texture of the film deposited at 200 °C was characterized by a low amount of the <111> component and a high amount of the random component. This is also consistent with the preferred growth model.

Post-deposition annealing was carried out in a vacuum furnace at 400 °C with a base pressure of 10^{-6} mbar, a partial H_2 pressure of 10 mbar, and under environmental conditions. The post-deposition grain growth was the same for annealing in high vacuum and in environmental conditions. A dramatic difference in the extent of growth was recognized in the micrographs of the 0.6 and 2.4 μm thick films. The 0.6 μm thick film showed normally grown grains with the <111> orientation; the average grain size was about 1 to 2 μm. This can be understood in light of the surface energy minimization. In contrast, in 2.4 μm thick films, abnormally large grains with the <001> orientation were found. These grains grew into the matrix of <111> grains. The grain boundaries between the abnormally grown grains have a meander-like shape unlike the usual polygonal shape. They could not explain the results by the model of Carel, Thomson, and Frost [27]. According to the model, the strain energy minimization favors the growth of <100> grains. The growth mode should be affected by strain and should not be sensitive to the initial texture. These predictions are at variance with the experimental results in which freestanding, stress-free films also showed abnormal growth of giant grains with <001> texture. The 2.4 μm thick films deposited at 100 °C or below could have dislocations whose density was high enough to cause Rex, which in turn gave rise to the texture change from <111> to <001> regardless of the existence of substrate when annealed, as explained in the previous section. Thus, the <111> to <100> texture change in the 2.4 μm thick films is compatible with SERM [28].

http://dx.doi.org/10.5772/54123

4. Axisymmetrically drawn fcc metals

It is known that the texture of axisymmetrically drawn fcc metals is characterized by major <111> + minor <100> components, and the drawing texture changes to the <100> texture after Rex [29,30]. Figure 16 shows calculated textures in the center region of 90% drawn copper wire taking work hardening per pass into account. The drawing to Rex texture transition was explained by SERM [4]. Since the drawing texture is stable, we consider the [111] and [100] fcc crystals representing the <111> and <100> fiber orientations constituting the texture. Figure 17 shows tetrahedron and octahedron consisting of slip planes (triangles) and slip directions (edges) for the [111] and [100] fcc crystals. The slip planes are not indexed to avoid complication. The slip-plane index can be calculated by the vector product of two of three slip directions (edges) of a triangle constituting the slip-plane triangle. It follows from Figure 17a that three active slip directions that are skew to the [111] axial direction are [101], [110], and [011]. It should be noted that these directions are chosen to be at acute angles with the [111] direction (Section 2). Therefore, AMSD // ([101] + [110] + [011]) = [222] // [111]. That is, AMSD is along the axial direction. According to SERM, AMSD in the deformed matrix is along MYMD in the Rexed grain. MYMDs of most of fcc metals are <100>. Therefore, the <111> drawing texture changes to the <100> Rex texture. Now, the evolution of <100> Rex texture in the <100> deformed matrix is explained. Eight active slip systems in fcc crystal elongated along the [100] direction are calculated to be (111)[1 0-1], (-111)[101], (1-1 1)[110], (1 1-1)[1-1 0], (111)[1-1 0], (-111)[110], (1-1 1)[10-1], and (1 1-1)[101], if the slip systems are {111}<110> [32]. It is noted that the slip directions are chosen to be at acute angles with the [100] axial direction. These slip systems are shown in Figure 17 b. AMSD is obtained, from the vector sum of the active slip directions, to be parallel to [100], which is also MYMD of fcc metals. Therefore, the <100> drawing texture remains unchanged after Rex (1st priority in Section 2), and the <111> + <100> orientation changes to <100> after Rex, regardless of relative intensity of <111> to <100> in the deformation texture. The <100> grains in deformed fcc wires are likely to act as nuclei for Rex. The texture change during annealing might take place by the following process. The <100> grains retain their deformation texture during annealing by continuous Rex, or by recovery-controlled processes, without long-range high-angle boundary migration. The <100> grains grow at the expense of their neighboring <111> grains that are destined to assume the <100> orientation during annealing.

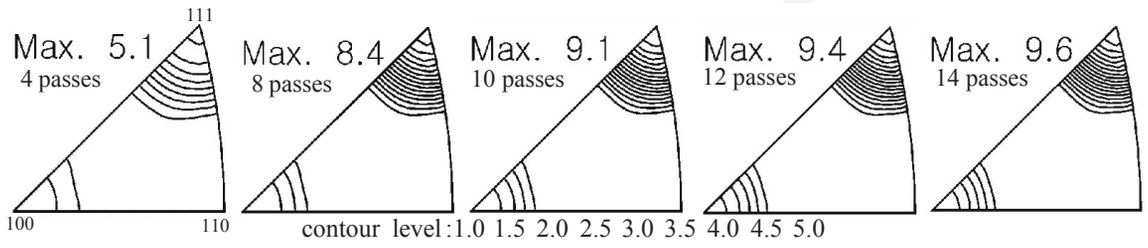

Figure 16. Calculated IPFs in centeral axis zone of Cu wire drawn by 90% in 14 passes (~15% per pass) through conical-dies of 9° in half-die angle, taking strain-hardening per pass into count [31].

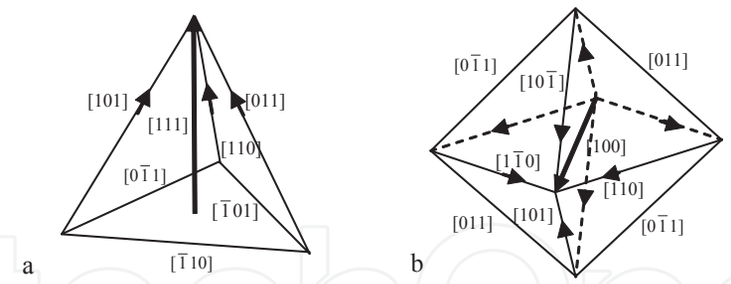

Figure 17. Tetrahedron and octahedron representing slip planes (triangles) and directions (edges) in [111] and [100] fiber oriented fcc crystals. Thick arrows show (a) [111] and (b) [100] axial directions.

4.1. Silver

Cold drawn Ag wires develop major <111> + minor <100> at low reductions (less than about 90%) as do other fcc metals, whereas they exhibit major <100> + minor <111> at high reductions (99%) as shown in Figure 18 [32]. This result is in qualitative agreement with that of Ahlborn and Wassermann [33], which shows that the ratio of <100> to <111> of Ag wires was higher at 100 and -196°C than at room temperature. They attributed the higher <100> orientation to Rex and mechanical twinning, because Ag has low stacking fault energy. They suggested that the <111> orientation transformed to the <115> orientation by twinning, which rotated to the <100> orientation by further deformation.

The hardness of deformed Ag wires as a function of annealing time at 250 and 300 °C indicated that Rex was completed after a few min. This was also confirmed by microstructure studies [32]. Figure 18 shows the annealing textures of drawn Ag wires of 99.95% in purity, which shows that drawing by 61 and 84% and subsequent annealing at 250 °C for 1 h gives rise to nearly random orientation. Ag wires with the <111> + <100> deformation texture develop Rex textures of major <100> and minor <111>, or major <100> + its twin component <122> and minor <111>. The almost random orientation can be seen in Figures 19 d. Figure 20 shows the IPFs of 99% drawn 99.99% Ag wire annealed at 600 ℃ for 1 min to 200 h. Their microstructures showed that the specimen annealed at 600 °C for 1min is almost completely Rexed. The specimen has major <100> + minor <111> as the specimens annealed at 300 °C. After annealing at 600 °C for 3min, some grains showed abnormal grain growth (AGG), indicating complete Rex, and the intensity of <100> component increased. However, as the annealing time incresed, the orientation density ratio (ODR) of <111> to <100> increased, accompanied by grain growth. It is noted that the annealing texture is diffuse at the transient stage from <100> to <111> (5 min in Figure 20 and Figure 19d). The <100> to <111> transition is associated with AGG in low dislocation-density fcc metals, which has been discussed in [31,32]. The Rex results before AGG lead to the conclusion that the Rex texture of the heavily drawn Ag wires is <100> regardless of relative intensity of <111> and <100>, as expected from SERM.

4.2. Aluminum, copper, and gold

Axisymmetrically extruded Al alloy rod [34], drawn Al wire [30] and Cu and some Cu alloy wires [29] generally have major <111> + minor <001> double fiber textures in the deformed

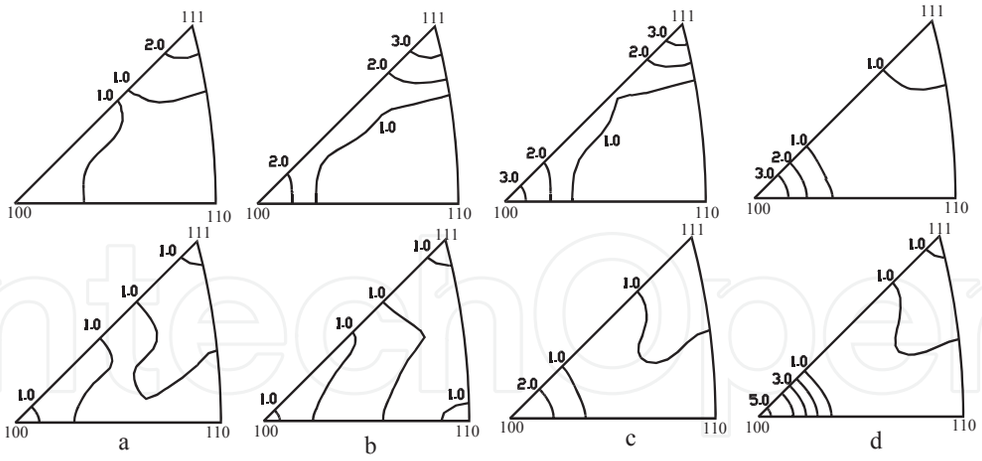

Figure 18. IPFs of (a) 61, (b) 84, (c) 91, and (d) 99% drawn Ag wires (initial texture: random) of 99.95% in purity (top) before and (bottom) after annealing at 250 °C for 1 h [32].

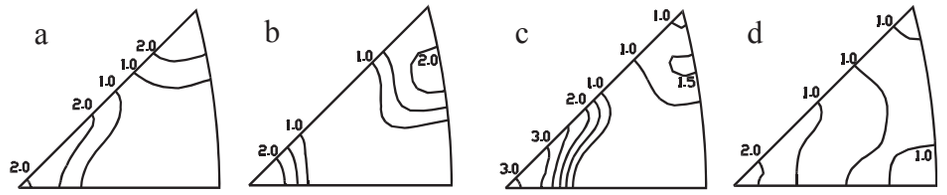

Figure 19. IPFs of 99.99% pure Ag wires (a) drawn by 90% and (b) annealed at 300 °C for 1 h; (c) drawn by 99% and (d) annealed at 300 °C for 1 h [32].

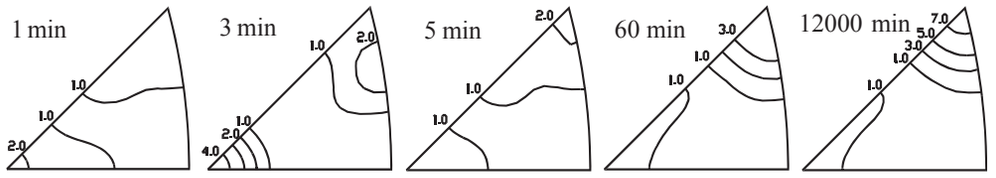

Figure 20. IPFs of 99.99% Ag wire drawn by 99% and annealed at 600 °C for 1-12000 min [32].

state. Park and Lee [35] studied drawing and annealing textures of a commercial electrolytic tough-pitch Cu of 99.97% in purity. A rod of 8mm in diameter, whose microstructure was characterized by equiaxed grains having a homogeneous size distribution, was cold drawn by 90% reduction in area in 14 passes through conical dies of 9° in half-die-angle with about 15% reduction per pass. The drawing speed was 10 m/min. The drawn wire was annealed in a salt bath at 300 or 600 °C and in air, argon, hydrogen or vacuum (< $1x10^{-4}$ torr) at 700 °C for various periods of time. Figure 21 shows orientation distribution functions (ODFs) for the 90% drawn Cu wire. The drawing texture can be approximated by a major <111> + minor <100> duplex fiber texture. The orientation density ratio of the <111> to <100> components is about 2.6. The orientation densities were obtained by averaging the f(g) values on the [φ_1=0-90°, Φ=0°,

φ_2=45°] line representing the <100> fiber texture and the [0-90°,55°,45°] line representing <111> in the φ_2=45° section of ODF. When annealed at 300 and 600 °C, the specimen developed textures of major <100> + minor <111> as expected from SERM. However, after annealing at 700 °C for 3 h, the grain size is so large that the ODF data consist of discrete orientations and the density of the <100> orientation is reduced while the density around the <1 1 1.7> orientation increases drastically. This is due to AGG and not discussed here. Wire drawing undergoes homogeneous deformation only in the axial center region, textures of the center regions were measured using electron backscatter diffraction (EBSD). The EBSD results are shown in Figure 22. The center region of the as-drawn specimen develops the major <111> + minor <100> fiber duplex texture as expected for axisymmetric deformation. The texture of the center region is similar to the gloval texure in Figure 21 because the deformation in wire drawing is relatively homogeneous. The annealing textures obtained at 700 °C is not the primary Rex texture.

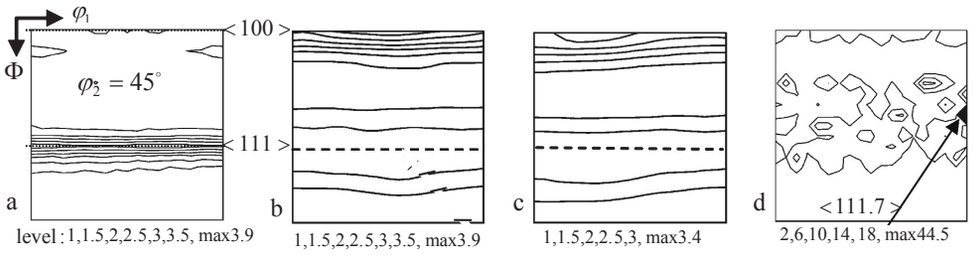

Figure 21. ODFs of 90% drawn Cu wire (a) before and after annealing at (b) 300, (c) 600, (d) 700 °C for 3 h, measured by X-ray [35].

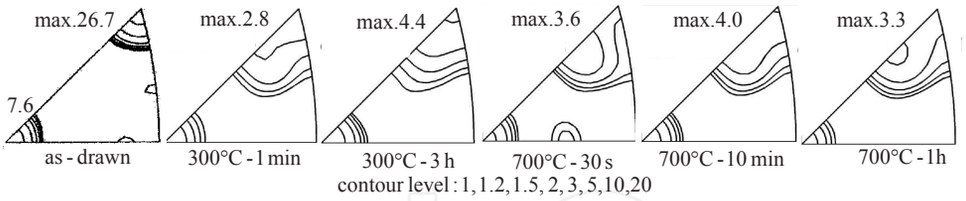

Figure 22. IPFs for center regions of 90% drawn Cu wires after annealing at 300 and 700°C [35].

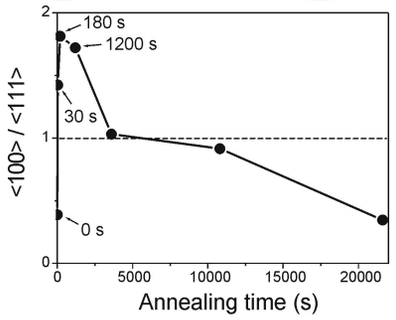

Figure 23. ODR of <100> to <111> of 90% drawn Cu wire vs. annealing time at 700°C [35].

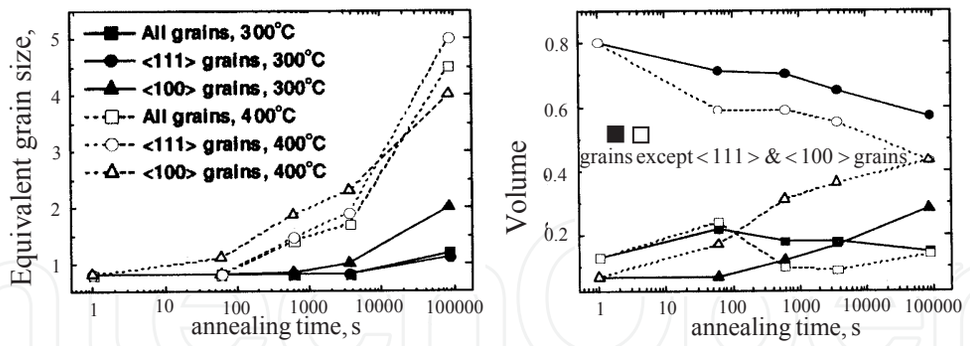

Figure 24. Grain size and volume fraction of ● ○ <111> and ▲△ <100> grains in Au wire vs. annealing time at 300 °C (solid symbols) and 400 °C (open symbols) [36].

Figure 23 shows ODR of <100> to <111> of the 90% drawn Cu wire as a function of annealing time at 700 °C. The ratio increases very rapidly up to about 1.8 after annealing for 180 s, wherefrom it decreases and reaches to about 0.3 after 6 h. The increase in the ratio indicates the occurrence of Rex and the decrease indicates the texture change during subsequent grain growth, that is, AGG. A similar phenomenon is observed in drawn Ag wire during annealing (Figure 20).

Cho et al. [36] measured the drawing and Rex textures of 25 and 30 μm diameter Au wires of over 99.99% in purity, which had dopants such as Ca and Be that total less than 50 ppm by weight. The Au wires were made by drawing through a series of diamond dies to an effective strain of 11.4.

Figure 24 shows the grain size and the volume fraction of the <111> and <100> grains as a function of annealing time at 300 and 400 °C. These values are based on EBSD measurements. The aspect ratio of grain shape was in the range of 1.5 - 2, which is little influenced by annealing time and temperature [36]. The grain growth occurs in whole area of the wire and is more rapid at 400 °C than at 300 °C as expected for thermally activated motion of grain boundaries. The volume fraction of the <111> grains decreases and that of the <100> grains increases with annealing time when Rex takes place, as expected from SERM.

5. Plane-strain compressed fcc metallic single crystals

5.1. Channel-die compressed {110}<001> aluminum single crystal

The annealing texture of single-phase crystals of Al-0.05% Si of the Goss orientation {110}<001> deformed in channel-die compression was studied by Ferry et al. [37]. In the channel-die compression, the compression and extension directions were <110> and <001> directions, respectively. Their experimental results showed that, even after deformation to a true strain of 3.0 which is equivalent to a compressive reduction of 95%, the original orientation was maintained as shown in Figure 25a. Figure 25b shows one (110) pole figure typical of a deformed crystal after annealing at 300 °C for 4 h. The comparison of Figures 25a and 25b suggests that the annealing texture is essentially the same as the deformation texture.

They also reported that even after 90% reduction and annealing for up to 235 h, the orientation was the same as that of the as-deformed crystal. For deformed specimens electropolished and annealed for various temperatures between 250 and 350 °C, no texture change took place before and after annealing, although grains which had different orientations were sometimes found to grow from the crystal surface after very long annealing treatments. For samples deformed over the true strain range of 0.5 to 3.0 in their work, annealing at a given temperature resulted in similar microstructural evolution. They called the phenomenon discontinuous subgrain growth during recovery. They stated that crystals of an orientation which was stable during deformation were generally resistant to Rex. This statement cannot be justified in light of single crystal examples in Sections 5.2 to 5.4.

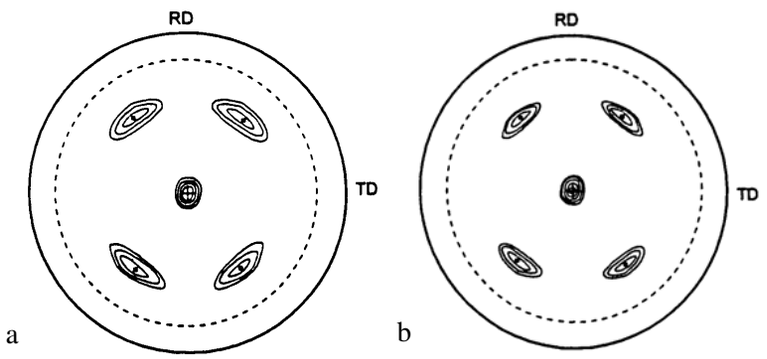

Figure 25. pole figures for 95% channel-die compressed Al single crystal (a) before and (b) after annealing at 300 ˚C for 4 h. (Contour levels: 2, 5, 11, 20, 35, 70 x random) [37].

The result was discussed based on SERM [38]. The (110)[001] orientation is calculated by the full constraints Taylor-Bishop-Hill model to be stable when subjected to plane strain compression. The active slip systems for the (110)[001] crystal are calculated to be (111)[0-1 1], (111)[-101], (-1-1 1)[011], and (-1-1 1)[101], whose activities are the same. It is noted that all the slip directions are chosen so that they can be at acute angle with the maximum strain direction [001]. AMSD is [0-1 1] + [-101] + [011] + [101] = [004]//[001], which is MYMD because $[S_{44}\text{-}2(S_{11}\text{-}S_{12})] < 0$ from compliances of Al [39]. When AMSD in the deformed state is parallel to MYMD in Rexed grains, the deformation texture remains unchanged after Rex (1st priority in Section 2).

5.2. Aluminum crystals of {123}<412> orientations

Blicharski et al. [40] studied the microstructural and texture changes during recovery and Rex in high purity Al bicrystals with S orientations, e.g. (123)[4 1-2]/(123)[-4-1 2] and (123)[4 1-2]/(-1-2-3)[4 1-2], which had been channel-die compressed by 90 to 97.5% reduction in thickness. The geometry of deformation for these bicrystals was such that the bicrystal boundary, which separates the top and bottom crystals at the midthickness of the specimen, lies parallel to the plane of compression, i.e. {123} and the <412> directions are aligned with the channel, and the die constrains deformation in the <121> directions. The annealing of the deformed bicrystals was conducted for 5 min in a fused quartz tube furnace with He + 5%H_2 atmosphere. The textures of the fully Rexed specimens were examined by determining the {111} and {200} pole figures from sectioned planes at 1/4, 1/2 and 3/4 specimen thickness. This roughly corresponds to

the positions at the midthickness of the top crystal, the bicrystal boundary, and the midthickness of the bottom crystal, respectively. The deformation textures of the two bicrystals, (123)[4 1-2]/(123)[-4-1 2] and (123)[4 1-2]/(-1-2-3)[4 1-2], channel-die compressed by 90%, are reproduced in Figure 26. The initial orientation of the component crystals is also indicated in these pole figures. The annealing textures are shown in Figure 27. As Bricharski *et al*. pointed out, the Rex textures of the fully annealed bicrystal specimens do not have 40° <111> rotational orientation relationship with the deformation textures (compare Figures 26 and 27). Lee and Jeong [41] dicussed the Rex textures based on SERM. The slip systems activated during deformation and their activities (shear strains on the slip systems) must be known. Figure 28 shows the orientation change of crystal {123}<412> during the plane strain compression. Comparing the calculated results with the measured values in Figure 28, the measured orientation change during deformation seems to be best simulated by the full constraints strain rate sensitivity model. Figure 29 shows the calculated shear strain increments on active slip systems of the (123)[4 1-2] crystal as a function of true thickness strain, when subjected to the plane strain compression. The experimental deformation texture is well described by (0.1534 0.5101 0.8463)[0.8111 0.4242 -0.4027], or (135)[2 1-1], which is calculated based on the full constraints strain rate sensitivity model with $m = 0.01$. The reason why the measured deformation texture is simulated at the reduction slightly lower than experimental reduction may be localized deformation like shear band formation occurring in real deformation. The localized deformation might not be reflected in X-ray measurements. The scattered experimental Rex textures may be related to the nonuniform deformation. Now that the shear strains on active slip systems are known, we are in position to calculate AMSD. For a true thickness strain of 2.3, or 90% reduction, the γ values (Eq. 8) of the (111)[1 0-1], (111)[0 1-1], (1-1 1)[110], (1-1-1)[110], (1-1 1)[011], and (1-1-1)[101] slip systems calculated using the data in Figure 29 are proportional to 2091, 776, 1424, 2938, 76, and 139, respectively. The contributions of the (1-1 1)[011] and (1-1-1)[101] slip systems are negligible compared with others. Therefore, the (111)[1 0-1], (111)[0 1-1], (1-1 1) [110], and (1-1-1)[110] systems are considered in calculating AMSD. It is noted that all the slip directions are chosen so that they can be at acute angle with RD, [0.8111 0.4242 -0.4027]. AMSD is calculated as follows:

$$209[10-1]+776[0\,1-1]+1424\times 0.577[110]+2938\times 0.577[110]=[4608\ 3293-2867]\,//\,[0.7259\ 0.5187-0.4516]\text{unit vector} \quad (12)$$

where the factor 0.577 originates from the fact that the slip systems of (1-1 1)[110] and (-111)[110] share the same slip direction [110] (Eq. 7). Two other principal stress directions are obtained as explained in Figure 6. Possible candidates for the direction equivalent to **S** in Figure 6 are the [011], [101], and [1-1 0] directions, which are not used in calculation of AMSD among six possible Burgers vector directions. The [011], [101], and [1-1 0] directions are at 87.3, 78.8 and 81.6°, respectively, with AMSD. The [011] direction is closest to 90° (Figure 30). The directions equivalent to **B** and **C** in Figure 6 are calculated to be [-0.0345 0.6833 0.7294] and [0.6869 -0.5139 0.5139] unit vectors, respectively. In summary, OA, OB, and OC in Figure 30, which are equivalent to **A**, **B**, and **C**, are to be parallel to the <100> directions in the Rexed grain. If the [0.7259 0.5187 -0.4516], [0.6869 -0.5139 0.5139] and [-0.0345 0.6833 0.7294] unit vectors are set to be parallel to [100], [010] and [001] directions after Rex (Figure 30), components of the unit vectors are direction cosines relating the deformed and Rexed crystal coordinate axes. Therefore, ND, [0.1534 0.5101 0.8463], and RD, [0.8111 0.4242 -0.4027], in the

deformed crystal coordinate system can be transformed to the expressions in the Rexed crystal coordinate system using the following calculations (refer to Eq. 9):

$$\begin{bmatrix} 0.7259 & 0.5187 & -0.4516 \\ 0.6869 & -0.5139 & 0.5139 \\ -0.0345 & 0.6833 & 0.7294 \end{bmatrix} \begin{bmatrix} 0.1534 \\ 0.5101 \\ 0.8463 \end{bmatrix} = \begin{bmatrix} -0.0062 \\ 0.2781 \\ 0.9606 \end{bmatrix} \tag{13}$$

$$\begin{bmatrix} 0.7259 & 0.5187 & -0.4516 \\ 0.6869 & -0.5139 & 0.5139 \\ -0.0345 & 0.6833 & 0.7294 \end{bmatrix} \begin{bmatrix} 0.8111 \\ 0.4242 \\ -0.4027 \end{bmatrix} = \begin{bmatrix} 0.9907 \\ 0.1322 \\ -0.0319 \end{bmatrix} \tag{14}$$

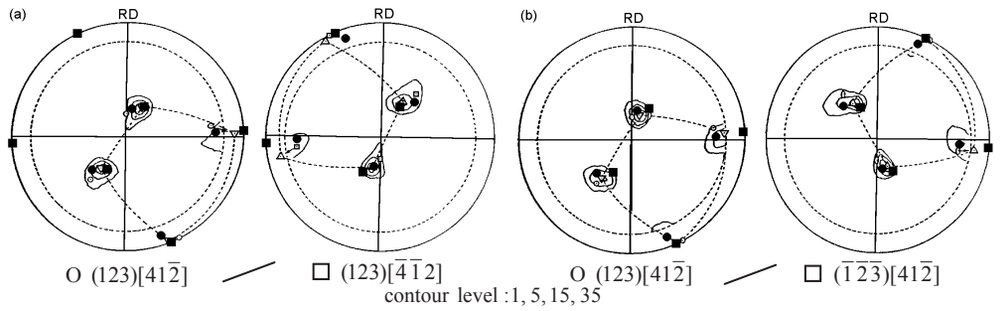

Figure 26. pole figures for 90% channel-die compressed Al crystals of {123}<412> orientations [40]. A/B indicates bi-crystal composed of A and B crystals. ● ~{135}<211>; ■ ~{011}<522>.

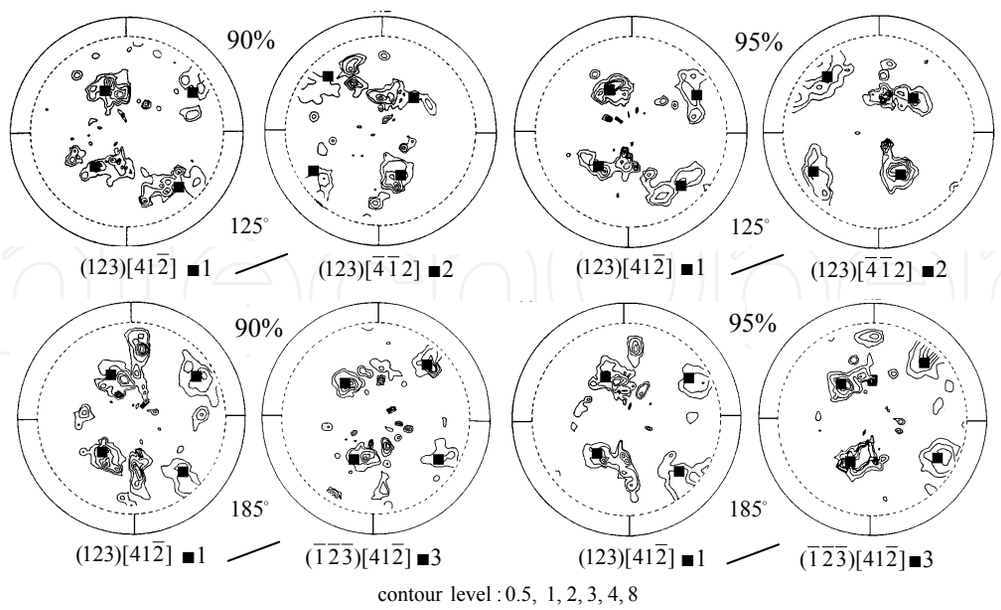

Figure 27. pole figures of 90 and 95% channel-die compressed Al bicrystals after annealing at 125 and 185 °C for 5 min [40]. ■ SERM-calculated Rex orientations: ■1 (-0.0062 0.2781 0.9606)[0.9907 0.1322 -0.0319]; ■2 (-0.0062 0.2781 0.9606)[-0.9907 -0.1322 0.0319]; ■3 (0.0062 -0.2781 -0.9606)[0.9907 0.1322 -0.0319] [41].

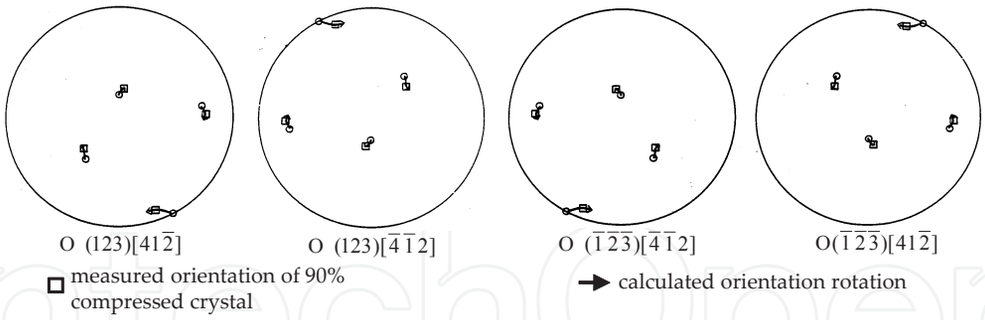

Figure 28. Orientation rotations of {123}<412> crystals during plain strain compression by 90% [41].

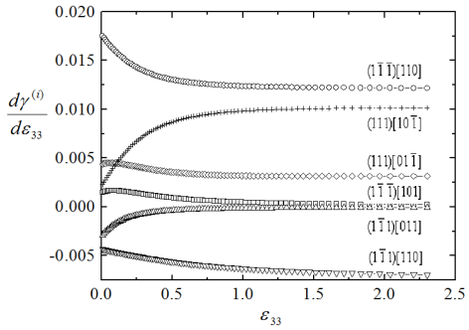

Figure 29. Calculated shear strain rate with respect to thickness reduction of 0.01, $d\gamma^{(i)}/d\varepsilon_{33}$, on active slip systems of (123)[4 1-2] crystal as a function of true thickness strain, $\varepsilon_{33,}$ [41].

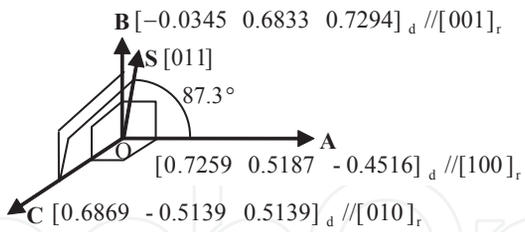

Figure 30. Orientation relations in deformed and Rexed states. Subscripts d and r indicate deformed state and Rexed state, respectively.

The calculated result means that the (0.1534 0.5101 0.8463)[0.8111 0.4242 -0.4027] crystal, which is obtained by the channel die compression by 90% reduction, transforms to the Rex texture (-0.0062 0.2781 0.9606)[0.9907 0.1322 -0.0319]. Similarly, crystals deformed by channel die compression from (123)[-4-1 2] and (-1-2-3)[4 1-2] orientations transform to (-0.0062 0.2781 0.9606)[-0.9907 -0.1322 0.0319] and (0.0062 -0.2781 -0.9606)[0.9907 0.1322 -0.0319], respectively, after Rex. The results are plotted in Figure 27 superimposed on the experimental data. It can be seen that the calculated Rex textures are in good agreement with the measured data.

5.3. Aluminum crystal of {112}<111> obtained by channel-die compression of (001)[110] crystal

Butler et al. [42] obtained a {112}<111> Al crystal by channel-die compression of the (001)[110] single crystal. The (001)[110]orientation is unstable with respect to plane strain compression, to form the (112)[1 1-1] and (112)[-1-1 1] orientations as shown in Figure 31a. The Rex texture produced after annealing at 200 °C was a rotated cube texture (Figure 31b). Lee [43] analyzed the result based on SERM. Figure 32 shows shear strains/extension strain on slip systems of 1 to 6 as a function of rotation angle about TD [-110] of the (001)[110] fcc crystal obtained from the Taylor-Bishop-Hill theory. The contribution of the slip systems to the deformation is approximated to be proportional to the area under the shear strains $\gamma^{(i)}$ on slip systems i / extension strain - rotation angle θ curve in Figure 32. The area ratio becomes

$$\int_0^{35}\gamma^{(1)}d\theta:\int_0^{10}\gamma^{(3)}d\theta:\int_{10}^{35}\gamma^{(5)}d\theta=30:3:20.6 \tag{15}$$

All the slips may not occur on the related slip systems uniformly in a large single crystal. Some regions of the crystal may be deformed by 1, 3, and 5 slip systems, while some other regions by 2, 4, and 6 slip systems.

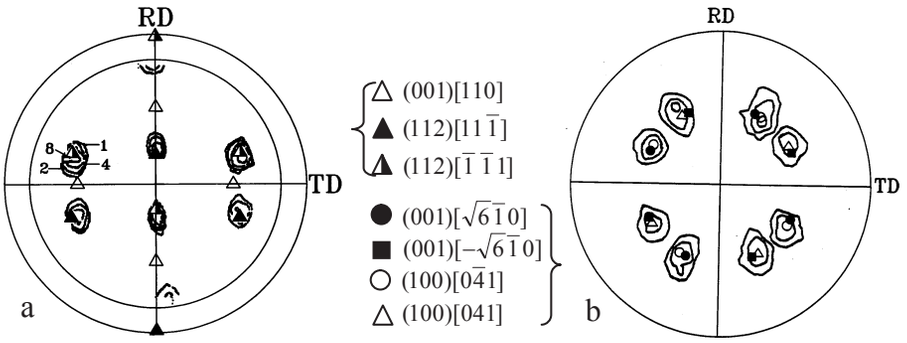

Figure 31. (a) (111) pole figure of Al single crystal with initial orientation (001)[110] after 70% reduction by channel-die compression; (b) (111) pole figure of measured Rex texture (contours), (100)[0-4 1], and (100)[041] [42]. (001)[√6 -1 0] and (001)[-√6 -1 0] are calculated by SERM [43].

For the contribution of the former three slip systems to the crystal deformation, AMSD is obtained by the vector sum of the [1 0-1], [0-1-1], and [110] directions whose contributions are assumed to be proportional to the area ratio obtained earlier (30 : 3 : 20.6). The vector sum is shown in Figure 33. The resultant direction passes through point E, which divides line BC by a ratio of 1 to 2. Thus, AMSD // AE // [3 1-2]. Another high stress direction equivalent to **S** in Figure 6 is BD, or [-110] which is not used in calculation of AMSD among possible Burgers vectors. The [-110] direction is not normal to AMSD. The direction that is at the smallest possible angle with the [-110] direction and normal to AMSD must be on a plane made of AMSD and the [-110] direction. The plane normal is obtained to be the [112] direction by the vector product of AMSD and the [-110] direction, which is equivalent to **C** in Figure 6. The

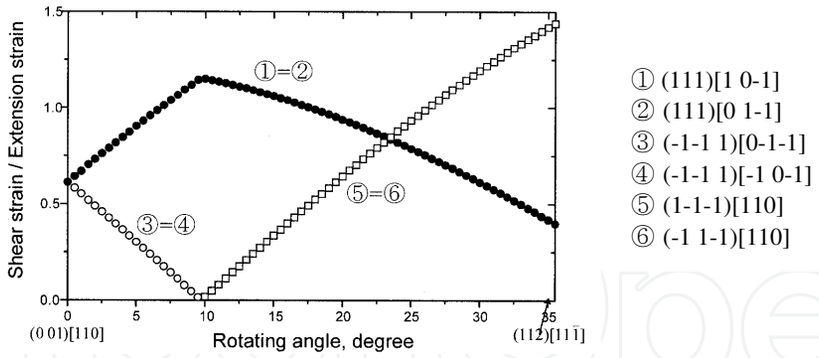

Figure 32. Shear strains on slip systems of 1 to 6 as a function of rotation angle about TD [-110] of (001)[110] crystal [43].

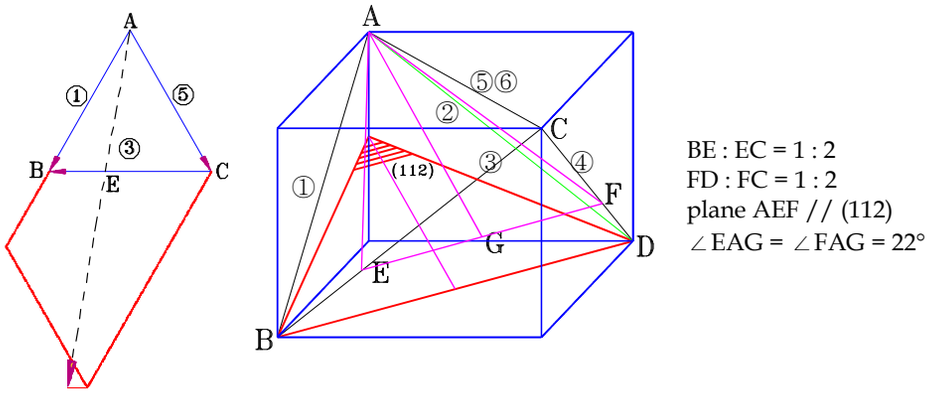

Figure 33. Vector sum of slip directions ① [1 0-1], ③ [0-1-1], and ⑤ [110] assuming that their activities are proportional to 30:3:20.6 (Eq. 15).

direction that is equivalent to **B** in Figure 6 is calculated to be [2-4 1] by the vector product of AMSD [3 1-2] and [112]. Thus, the [3 1-2], [2-4 1], and [112] directions become parallel to <100> in the Rexed grains.

If the directions [3 1-2], [2-4 1], and [112], whose unit vectors are [3/√14 1/√14 -2/√14], [2/√21 -4/√21 1/√21], and [1/√6 1/√6 2/√6], respectively, are set to be parallel to [100], [010] and [001] directions in the Rexed crystal, components of the unit vectors are direction cosines relating the deformed and Rexed crystal coordinate axes (Eq. 9). Therefore, ND, [112], and RD, [1 1-1], in the deformed crystal coordinate system can be transformed to the expressions in the Rexed crystal coordinate system using the following calculation:

$$\begin{bmatrix} 3/\sqrt{14} & 1/\sqrt{14} & -2/\sqrt{14} \\ 2/\sqrt{21} & -4/\sqrt{21} & 1/\sqrt{21} \\ 1/\sqrt{6} & 1/\sqrt{6} & 2/\sqrt{6} \end{bmatrix} \begin{bmatrix} 1 \\ 1 \\ 2 \end{bmatrix} // // \begin{bmatrix} 0 \\ 0 \\ 1 \end{bmatrix} \quad \text{and} \quad \begin{bmatrix} 3/\sqrt{14} & 1/\sqrt{14} & -2/\sqrt{14} \\ 2/\sqrt{21} & -4/\sqrt{21} & 1/\sqrt{21} \\ 1/\sqrt{6} & 1/\sqrt{6} & 2/\sqrt{6} \end{bmatrix} \begin{bmatrix} 1 \\ 1 \\ -1 \end{bmatrix} // // \begin{bmatrix} \sqrt{6} \\ -1 \\ 0 \end{bmatrix}$$

Therefore, the (112)[11-1] deformation texture transforms to the (001)[√6-1 0] Rex texture. Similarly, from the (111)[0 1-1], (-1-1 1)[-1 0-1], and (-1 1-1) [110] slip systems, another AMSD AF, or

the [1 3-2] direction, can be obtained. In this case, the (112)[1 1-1] deformation texture transforms into the (001)[-√6 -1 0] Rex texture. The {001}<√6 1 0> orientation has a rotational relation with the {001}<100> orientation through 22° about the plane normal. The calculated Rex texture is superimposed on the measured data in Figure 31b. The calculated results are in relatively good agreement with the measured data. It is noted that Figure 32 does not represent the correct strain path during deformation. Therefore, there is a room to improve the calculated Rex texture. The Rex texture is at variance with the {001}<100> Rex texture in polycrystalline Al and Cu.

5.4. Copper crystal of (123)[-6-3 4] in orientation rolled by 99.5% reduction in thickness

Kamijo et al. [44] rolled a (123)[-6-3 4] Cu single crystal reversibly by 99.5% under oil lubrication. The (123)[-6-3 4] orientation was relatively well preserved up to 95%, even though the orientation spread occurred as shown in Figure 34a. However, the crystal rotation proceeded with increasing reduction. A new (321)[-4 3 6] component, which is symmetrically oriented to the initial (123)[-6-3 4] with respect to TD, developed after 99.5% rolling as shown in Figure 34b. It is noted that other two equivalent components are not observed. The rolled specimens were annealed at 538 K for 100 s to obtain Rex textures. In the Rex textures of the crystals rolled less than 90%, any fairly developed texture could not be observed, except for the retained rolling texture component. They could observe a cube texture with large scatter in the 95% rolled crystal and the fairly well developed cube orientation in the 99.5% rolled crystal after Rex as shown in Figure 34c. They concluded that the development of cube texture in the single crystal of the (123)[-6-3 4] orientation was mainly attributed to the preferential nucleation from the (001)[100] deformation structure. The cube deformation structure was proposed to form due to the inhomogeneity of deformation. Lee and Shin [45] explained the textures in Figure 34 based on SERM. Figure 35 shows $d\gamma^{(i)}/d\varepsilon_{11,}$ with $d\varepsilon_{11}$ = 0.01, on active slip systems i as a function of ε_{11} for the (123)[-6-3 4] crystal, which was calculated by the $d\varepsilon_{13}$ and $d\varepsilon_{23}$ relaxed strain rate sensitive model (m = 0.02) with the subscripts 1, 2, and 3 indicating RD, TD, and ND. The changes in $d\gamma^{(i)}/d\varepsilon_{11}$ depending on ε_{11} indicate that the (123)[-6-3 4] orientation is unstable with respect to the plane strain compression. A part of the (123)[-6-3 4] crystal, particularly the surface layers where $d\varepsilon_{23}$ is negligible due to friction between rolls and sheet, seems to rotate to the {112}<111> orientation. A part of the {112}<111> crystal further rotates to (321)[-436] with increasing reduction. This is why (321)[-436] has lower density than (123)[-6-3 4] along with weak {112}<111>. The orientation rotation is shown in Figure 35b. Since important components in the deformation texture are (123)[-6-3 4], (321)[-436], and {112}<111>, their Rex textures are calculated using SERM. If the (123)[-6-3 4] orientation is stable, $d\gamma^{(i)}/d\varepsilon_{11}$ on the active slip systems do not vary with strain. It follows from Fig. 35a that $d\gamma^{(i)}/d\varepsilon_{11}$ on C, J, M, and B are 0.014, 0.01, 0.007, and 0.003, respectively, at zero strain. Therefore, AMSD is 0.014 [-101] + 0.01×0.577 [-1-1 0] + 0.007 ×0.577 [-1-1 0] + 0.003 [0-1 1] = [-0.02381 -0.01281 0.017], where the factor 0.577 originates from the fact that the duplex slip systems of (1-1 1)[-1-10] and (-111) [-1-10] share the same slip direction (Figure 4). The [-0.02381 -0.01281 0.017] direction, or the [-0.745 -0.401 0.532] unit vector, will be parallel to one of the <100> directions, MYMDs of Cu, after Rex. Orientation relationship between the matrix and Rexed state is shown in Figure 36a, which is obtained as explained in Figure 6. The Rex orientation of the (123)[-6-3 4] matrix is calculated as follows:

$$\begin{pmatrix} -0.745 & -0.401 & 0.532 \\ 0.069 & 0.747 & 0.660 \\ -0.663 & 0.529 & -0.529 \end{pmatrix} \begin{pmatrix} 1 \\ 2 \\ 3 \end{pmatrix} = \begin{pmatrix} 0.049 \\ 3.543 \\ -1.192 \end{pmatrix} \text{ and } \begin{pmatrix} -0.745 & -0.401 & 0.532 \\ 0.069 & 0.747 & 0.660 \\ -0.663 & 0.529 & -0.529 \end{pmatrix} \begin{pmatrix} -6 \\ -3 \\ 4 \end{pmatrix} = \begin{pmatrix} 7.801 \\ -0.017 \\ -0.275 \end{pmatrix}$$

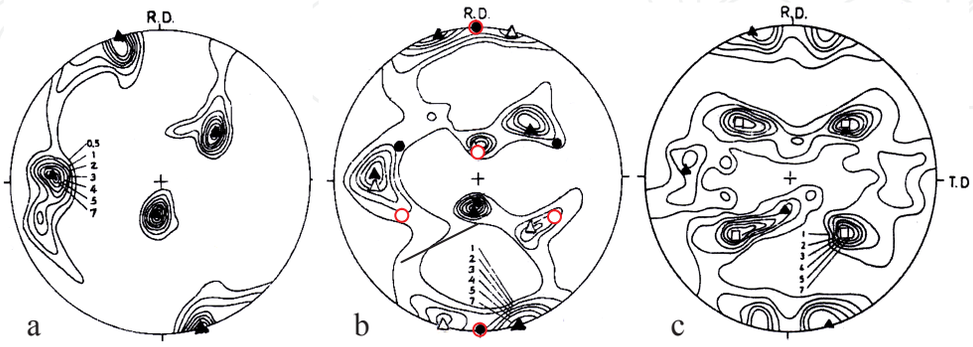

Figure 34. pole figures for (123)[-6-3 4] Cu single crystal after rolling by (a) 95%, (b) 99.5%, and (c) 99.5% and subsequent annealing at 538 K for 100 s [44]. ▲(123)[-6-3 4]; Δ(321)[-436]; ●(112)[-1-1 1]; ○ (112)[11-1]; □(001)[100].

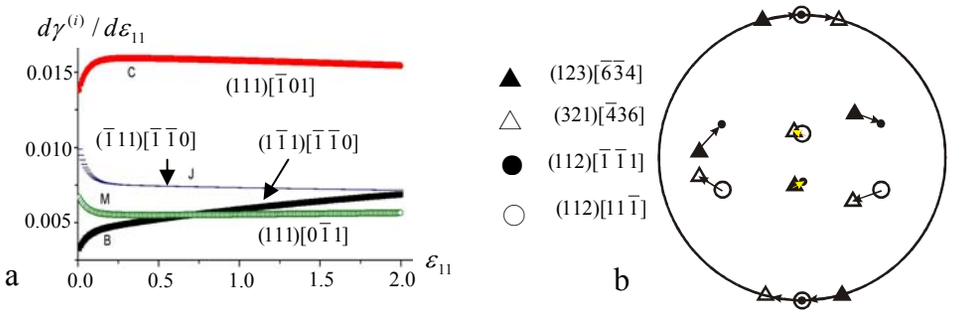

Figure 35. (a) Shear strain rates $d\gamma/d\varepsilon_{11}$ with $d\varepsilon_{11}$=0.01 vs. ε_{11} on active slip systems (C, J, M, B) and (b) (111) pole figure showing orientation rotation from {123}<634> to {112}<111> [45].

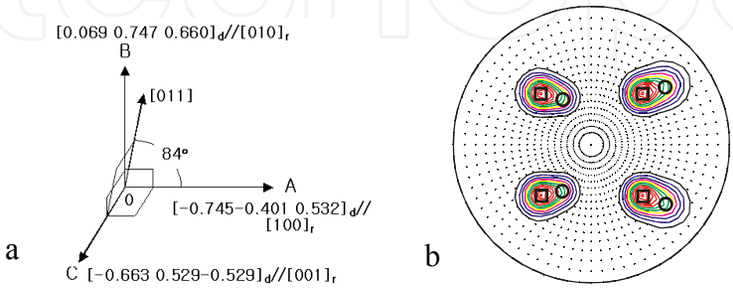

Figure 36. a) Orientation relationship between deformed ($_d$) and Rexed ($_r$) states and (b) (111) pole figures of ○ (0 3-1) [100] and □ (001)[100] orientations. Contours were calculated assuming Gaussian scattering (10°) of (0 3-1)[100] and (001)[100] components with their density ratio being 2:1 [45].

The calculated Rex orientation is (0.049 3.543–1.192)[7.801-0.017-0.275] ≈ (0 3-1)[100]. Similarly the (321)[-436] crystal is calculated to have slip systems of (111)[-101], (111)[-110], (-1-1 1)[011], and (-1 1-1)[011], on which the shear strain rates at $d\varepsilon_{11}$=0 are 0.014, 0.003, 0.01, and 0.007, respectively. The (321)[-436] is calculated to transform to the (-0.049 3.543-1.192)[7.801 0.017 -0.275] ≈ the (0 3-1)[100] Rex texture. This result is understandable from the fact that the (0 3-1) [100] orientation is symmetrical with respect to TD as shown in Figure 36b and the deformation orientations, (123)[-6-3 4] and (321)[-436], are also symmetrical with respect to TD as shown in Figure 35b. The {112}<111> rolling orientation to the {001}<100> Rex orientation transformation is discussed based on SERM in Section 6.1.

According to the discussion in Section 6.1, if the cube oriented regions are generated during rolling, they are likely to survive and act as nuclei and grow at the expense of neighboring {112}<111> region during annealing because the region tend to transform to the {001}<100> orientation to reduce energy. The grown-up cube grains will grow at the expense of grains having other orientations such as the {123}<634> orientation, resulting in the {001}<100> texture after Rex, even though the Cu orientation is a minor component in the deformation texture. Meanwhile, the main S component in the deformation texture can form its own Rex texture, the near (0 3-1)[100] orientation. In this case, the Rex texture may be approximated by main (001)[100] and minor (0 3-1)[001] components. Figure 36b shows the texture calculated assuming Gaussian scattering (half angle=10°) of these components with the intensity ratio of (001)[100]: (0 3-1)[001] = 2 : 1. It is interesting to note that the cube peaks diffuse rightward under the influence of the minor (0 3-1)[100] component in agreement with experimental result in Figure 34c.

6. Cold-rolled polycrystalline fcc metals and alloys

6.1. Cube recrystallization texture

The rolling texture of fcc sheet metals with medium to high stacking fault energies is known to consist of the brass orientation {011}<211>, the Cu orientation {112}<111>, the Goss orientation {011}<100>, the S orientation {123}<634>, and the cube orientation {100}<001>. The fiber connecting the brass, Cu, and S orientations in the Euler space is called the β fiber. Major components of the plane-strain rolling texture of polycrystalline Al and Cu are known to be the Cu and S orientations. The Rex texture of rolled Al and Cu sheets is well known to be the cube texture. The 40°<111> orientation relationship between the S texture and the cube texture has been taken as a proof of OG, and has made one believe that the S orientation is more responsible for the cube Rex texture. OG is claimed to be associated with grain boundary mobility anisotropy. However, experimental data indicate that the Cu texture is responsible for the cube texture. For an experimental result of Table 3, the deformation texture is not strongly developed below a reduction of 73% and its Rex texture is approximately random. At a reduction of 90%, a strong Cu texture is obtained and its Rex texture is a strong cube texture. For 95% cold rolled Al-0 to 9%Mg alloy after annealing at 598K for 0.5 to 96 h, the highest density in the Cu component in the deformation texture and the highest density in the

cube component in Rex textures were observed at about 3% Mg (Figure 37). This implies that the Cu component is responsible for the cube component. However, these cannot prove that the Cu texture is responsible for the cube texture because deformation components with the highest density are not always linked with highest Rex components [47].

Changes in orientation densities of 95% rolled Cu during annealing at 400 to 500 °C (Figure 38), 95% rolled AA8011 Al alloy during annealing at 350 °C (Figure 39a), and 95% rolled Fe-50%Ni alloy during annealing at 600℃ (Figure 39b), and 95% rolled Cu after heating to 150 to 300℃ at a rate of 2.5 K/s followed by quenching showing that the Cu component disappears most rapidly when the cube orientation started to increase [52]. These results imply that the Cu component is responsible for the cube Rex texture. Rex is likely to occur first in high strain energy regions. It is known that the energy stored in highly deformed crystals is proportional to the Taylor factor ($\Sigma d\gamma^{(k)}/d\varepsilon_{ij}$ with γ and ε_{ij} being shear strains on slip systems k and strains of specimen, respectively). The Taylor factor is calculated to be 2.45 for the cube oriented fcc crystal using the full constraints model, 3.64 for the Cu oriented fcc crystal using the ε_{13} relaxed constraints rate sensitive model, 3.24 for the S oriented fcc crystal using the ε_{13} and ε_{23} relaxed constraints rate sensitive model, and 2.45 for the brass orientation using the ε_{12} and ε_{23} relaxed constraints rate sensitive model. In the rate sensitive model calculation, the rate sensitivity index was 0.01 and each strain step in rolling was 0.025. The measured stored energies for 99.99% Al crystals channel-die compressed by a strain of 1.5 showed that the Cu oriented region had higher energies than the S oriented region [53]. The Taylor factors and the measured stored energies indicate that the driving force for Rex is higher in the Cu oriented grains than in the S oriented grains. Therefore, the Cu component in the deformation texture is more responsible for the cube Rex texture than the S component.

	Rolling reduction	Brass	Copper	Goss	S	Cube
Rolling texture	58%	3.6	2.6	1.1	1.4	0.6
	73%	2.8	3.0	0.9	1.1	1.1
	90%	0.7	5.7	0.1	0.7	1.3
Rex texture	58%	2.1	1.4	1.0	1.3	1.2
	73%	1.8	1.5	1.3	1.4	2.1
	90%	0.2	0.8	0.2	0.4	20.0

Table 3. Texture component strength of high purity OFE copper [46]

The copper to cube texture transition was first explained by SERM [4], and elaborated later [54]. The orientations of the (112)[1 1-1] and (123)[6 3-4] Cu single crystals remain stable in the center layer for all degree of rolling [55]. The Cu orientation (112)[1 1-1] is calculated to be stable by the ε_{13} relaxed constraint model [56,57]. For the (112)[1 1-1] crystal, the active slip systems are calculated by the RC model to be (-1 1-1)[110], (1-1-1)[110], (111)[1 0-1], and (111)[0 1-1], on which shear strain rates are the same regardless of reduction ratio. Almost the same

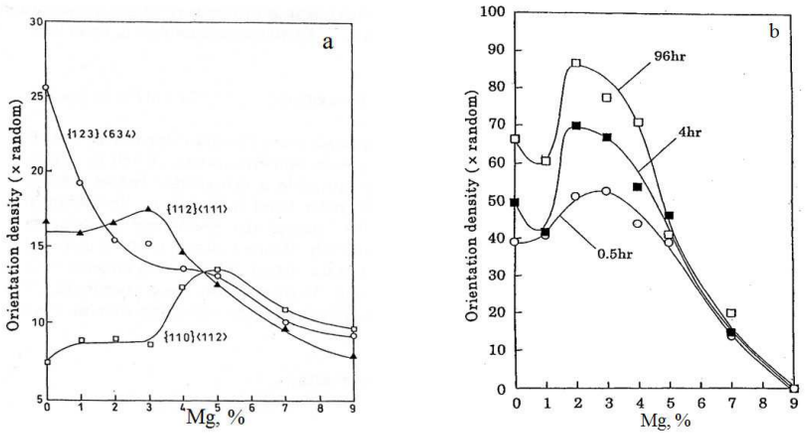

Figure 37. Effect of Mg content on (a) densities of {112}<111>, {123}<634>, and {110}<112> orientations in Al-Mg alloys cold rolled by 95% and on (b) density of {001}<100> orientation in specimens annealed at 598 K for 0.5, 4, and 96 h [48].

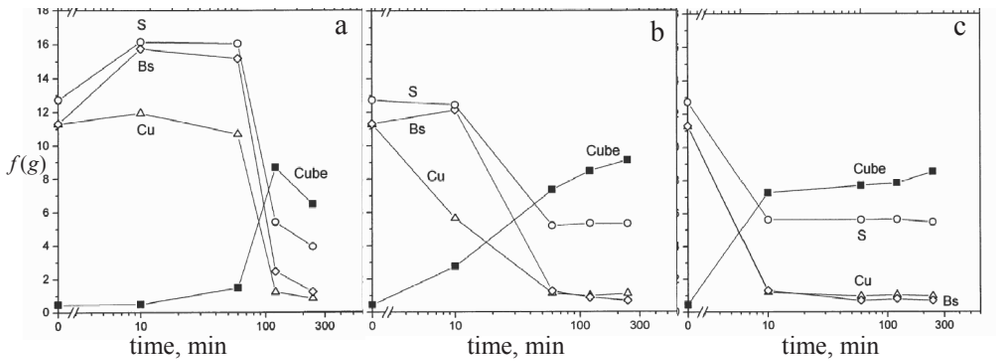

Figure 38. Changes in densities of copper Cu, S, brass Bs, and cube orientations in 95% cold rolled copper during annealing at (a) 400, (b) 450, and (c) 500 °C [49].

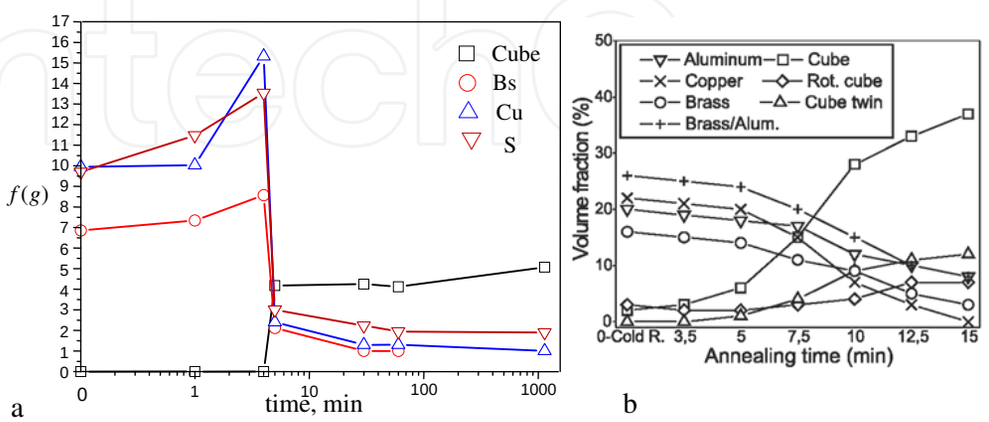

Figure 39. a) Changes in densities of cube, brass, copper and S orientations in 95% cold-rolled AA8011 Al alloy during annealing at 350 °C [50]. (b) Evolution of bulk textures in 90% cold-rolled Fe-50%Ni alloy during annealing at 600 °C [51].

result is obtained by ε_{13}, ε_{23} relaxed constraints rate sensitive model [54]. The slip directions are chosen to be at acute angles with RD (Section 2). To calculate AMSD, the active slip systems are weighted by the shear strain rates on them. AMSD is calculated to be [0 1-1] + [1 0-1] + 0.577 × 2[110] ≈ 2 [1 1-1]. Here the factor 0.577 is related to the fact that the slip direction [110] is shared by the (-1 1-1) and (1-1-1) slip planes (Eq. 7). The [1 1-1] direction is equivalent to **A** in Figure 6. **S** becomes [1-1 0] because it is one of slip directions nearest to 90° with **A**. In fact. **S** is normal to **A**, so **S** becomes **B** and **C** = **A**×**B** = [-1-1-2]. Since MYMDs are <100>, the Rex orientation is calculated using Eq. 9 to be (0 0-1)[100], which is equivalent to (001)[100]. In conclusion, the (112)[1 1-1] deformation texture is calculated to change to the (001)[100] Rex texture.

The above calculation indicates that the Cu orientation tends to turn into the cube orientation during annealing. In order for the transformation to occur, the cube oriented nuclei are needed, whether they may be generated from the deformed matrix or already existing cube bands. In order for the cube bands to be nuclei, they must be stable during annealing. The cube orientation (001)[100] is calculated by the full constrains method to be metastable with respect to plane strain compression, with active slip systems being (111)[1 0-1], (1 1-1)[101], (1-1-1)[101], and (1-1 1)[1 0-1] on which the shear strain rates are the same. If cube oriented grains survive after rolling, they must have undergone the plane strain compression with the slip systems. Therefore, AMSD is [1 0-1] + [101] + [101] + [1 0-1] = [400] // [100]. This is MYMD of Cu. Since AMSD is the same as the MYMD, the cube texture is expected to remain unchanged whether Rex or recovery (1st priority in Section 2).

SERM does not tell us how the cube oriented nuclei form. If the cube oriented grains survived during rolling, they are likely to survive and act as nuclei and grow at the expense of neighboring Cu oriented grains during annealing, because the Cu oriented grains tend to transform to the cube orientation. The grown up cube grains will grow at the expense of grains having other orientations such as the S and brass orientations, resulting in the cube texture after Rex. This discussion applies to other fcc metals with high stacking fault energy (SFE).

6.2. Goss recrystallization texture

The evolution of rolling textures in copper alloys depends strongly on their SFEs. A continuous transition from the copper orientation to the brass orientation tends to occur with increasing content of alloying elements or decreasing SFE. However, Mn can be dissolved in copper up to 12 at.% without significantly changing SFE unlike various Cu alloys [58]. Engler [59,60] studied the influence of Mn on the deformation and Rex behavior of Cu-4 to 16%Mn alloys, as this should yield a clear separation of the effects caused by the changes in SFE from those due to other factors. It is particularly interesting that the alloys develop a deformation texture in which the density of the brass orientation can be higher than the densities of the copper orientation and the S orientation despite the fact that SFEs of the alloys are almost the same as that of pure Cu. The brass orientation is obtained in many Cu alloys with low SFEs, which is well known to transforms to the {236}<385> orientation. However, the Cu-Mn alloys do not develop the {236}<385> orientation after Rex. The texture transformation cannot be well explained by 40° <111> relation between the deformation and Rex textures.

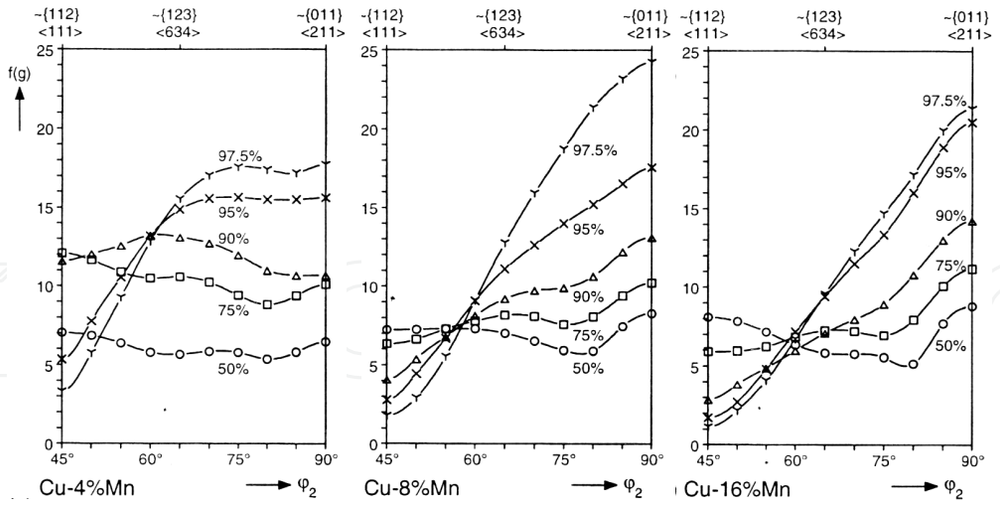

Figure 40. β-fiber intensity lines of Cu-4%Mn, Cu-8%Mn, and Cu-16%Mn alloys after rolling reductions from 50 to 97.5% [59].

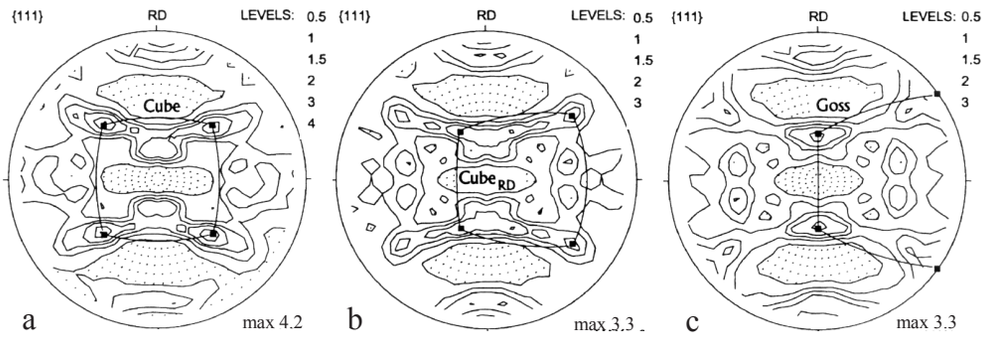

Figure 41. pole figures of (a) Cu-4%Mn, (b) Cu-8%Mn, and (c) Cu-16%Mn alloys after complete Rex (97.5% rolling, annealing for 1000 s at 450 °C) [60].

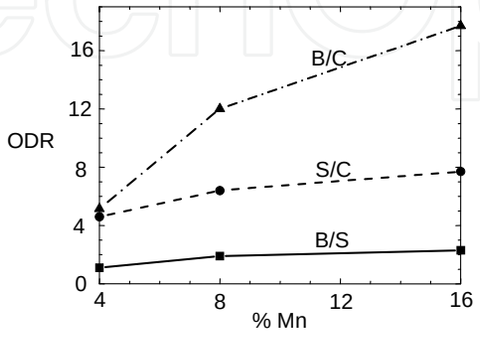

Figure 42. Orientation density ratios (ODR) among brass B, S, and copper C components in rolling texture (Figure 40) as a function of Mn concentration in Cu-Mn alloy [61].

http://dx.doi.org/10.5772/54123

Figure 40 shows the orientation densities f(g) along the β-fiber of Cu-4%Mn, Cu-8%Mn, and Cu-16%Mn alloys after rolling reductions of 50 to 97.5%. The figure indicates that with increasing Mn content and rolling reduction the brass orientation tends to dominate the rolling texture. The brass orientation in the Cu-Mn alloys is particularly interesting because the transformation of the orientation to the Rex texture will not be complicated by twinning as in low SFE alloys. Figure 41 shows {111} pole figures of the three Cu-Mn alloys rolled by 97.5% after complete Rex by annealing for 1000 s at 450 °C. In Cu-4%Mn the texture maximum lies in the cube-orientation. In Cu-8%Mn the texture maximum has shifted from the cube orientation to an orientation which can be approximated by the {013}<100> orientation. In Cu-16%Mn the texture maximum is in the Goss orientation. The orientation density ratios among the copper, S, and brass components in the rolling texture are shown in Figure 42. The density ratio of the brass to S component increases from about 1 to 2, the density ratio of the S to copper component increases from about 5 to 8, and the density ratio of the brass to copper component increases from about 5 to 18 with increasing Mn content from 4 to 16% in the Cu- Mn alloy. The density ratio of the S to copper and that of the brass to copper component are lowest in 4%Mn and highest in 16%Mn.

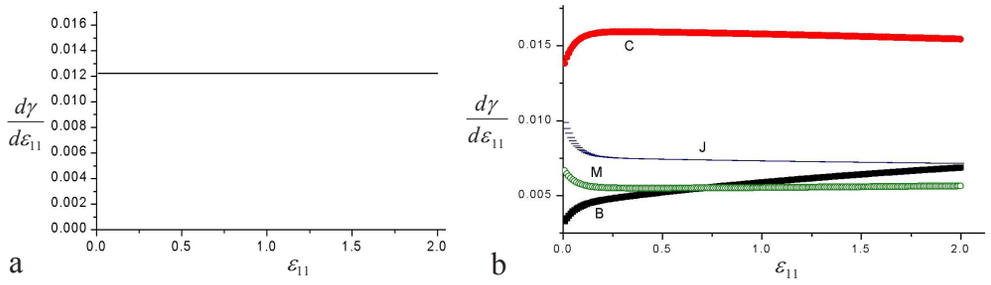

Figure 43. $d\gamma/d\varepsilon_{11}$ ($d\varepsilon_{11}$=0.01) vs. ε_{11} curves on active slip systems of (a) (111)[0-1 1] and (-1-1 1)[101] of (110)[1-1 2] crystal and of (b) J (1-1-1)[110], B (111)[0 1-1], M (-1 1-1)[110], and C (111)[1 0-1] of (123)[6 3-4]. Values of $d\gamma/d\varepsilon_{11}$ on B, M, J, and C are 0.003, 0.006, 0.01, and 0.014, respectively, at ε_{11}=0 [61].

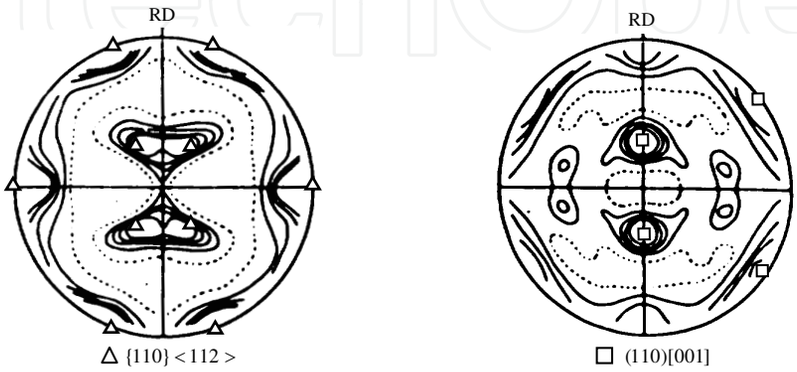

Figure 44. {110}<112> rolling and {110}<001> Rex textures of Cu-1% P alloy [62].

Comparison of the Rex textures with the corresponding deformation textures indicates that the brass component in the deformation texture seems to be responsible for the Goss components in the Rex texture. In what follows, the Rex textures are discussed based on SERM [61]. In order to find which component in the rolling texture is responsible for the Goss Rex texture, the brass rolling texture is first examined because it is the highest component in the deformation texture of Cu-16% Mn alloy, which changed to the Goss texture when annealed. When fcc crystals with the (110)[1-1 2] orientation are plane strain compressed along the [110] direction and elongated along the [1-1 2] direction, the relation between the strain ε_{11} of specimen and shear strain rates $d\gamma/d\varepsilon_{11}$ on active slip systems was calculated by the ε_{13} and ε_{23} relaxed strain rate sensitive model. Figure 43a shows the calculated results, which indicate that active slip systems are (111)[0-1 1] and (-1-1 1)[101] and their shear strain rates do not vary with strain of specimen indicating that the brass orientation is stable with respect to the strain. It is noted that the active slip directions were chosen to be at acute with the [1-1 2] RD. Thus, AMSD = [0-1 1] + [101] = [1-1 2] is the same as RD.

According to SERM, AMSD is parallel to MYMD of Rexed grain, the <100> directions in fcc metals. Therefore, the Rexed grains will have the (hk0)[001] orientation. The 2nd priority in Section 2 gives rise to the (110)[001] orientation because the (110) plane is shared by the deformed and Rexed grains. That is, the (110)[1-1 2] rolling texture transforms to the (110)[001] Rex texture. Similarly, for the (011)[2-1 1] crystal, equally active slip systems of (111)[1-1 0] and (1-1-1)[101] are obtained. Therefore, the (011)[2-1 1] rolling texture is calculated to transform to the (011)[100] Rex texture. It is concluded that the Goss Rex texture is linked with the brass rolling texture. The Goss orientation is stable with respect to plane strain compression and thermally stable (Section 5.1). Therefore, the Goss grains that survived during rolling are likely to act as nuclei during subsequent Rex and will grow at the expense of surrounding brass grains which are destined to change to assume the Goss orientation.

Figure 44 shows the rolling and Rex textures of Cu-1% P alloy sheet. The {110}<112> rolling texture changes to the (110)[001] texture after Rex. This is another example of the transition from the {110}<112> rolling texture to the {110}<001> Rex texture as explained in the Cu-16% Mn alloy.

6.3. {031}<100> recrystallization texture

In Section 5.4 the (123)[-6-3 4] rolling to (031)[100] Rex orientation transformation was discussed. Here we discuss the {123}<634> rolling to {031}<100> Rex orientation transformation. Figure 43b shows the shear strain rates as a function of strain for the (123)[6 3-4] crystal, which was calculated by the ε_{13} and ε_{23} relaxed strain rate sensitive model. The figure indicates that the S orientation is not stable with respect to the strain. Therefore, we calculate AMSD using the shear strain rates of 0.014, 0.01, 0.006 (0.007 was used in Section 5.4), and 0.003 at zero strain on the C, J, M, and B active slip systems (Figure 43b). AMSD is 0.014 [10-1] + 0.01 ×0.577 [110] + 0.006 × 0.577 [110] + 0.003 [0 1-1] = [0.023 0.0122 –0.017], where the factor 0.577 originates from the fact that the (1-1 1) and (1-1-1) slip planes share the [110] slip direction (Eq. 7). The [0.023 0.0122 –0.017] AMSD is parallel to the [0.7397 0.3924 –0.5467] unit vector. Following the method explained in Figure 6, we obtain Figure 45. Therefore, the (123)[6 3-4] rolling orientation is calculated to transform to the Rex texture as explained in Eq. 9. The calculated results are as follows:

$$\begin{pmatrix} 0.7397 & 0.3924 & -0.5467 \\ 0.0812 & 0.7545 & 0.6513 \\ 0.6684 & -0.5263 & 0.5263 \end{pmatrix}\begin{pmatrix} 1 \\ 2 \\ 3 \end{pmatrix}=\begin{pmatrix} -0.1156 \\ 3.5441 \\ 1.1947 \end{pmatrix} \quad \begin{pmatrix} 0.7397 & 0.3924 & -0.5467 \\ 0.0812 & 0.7545 & 0.6513 \\ 0.6684 & -0.5263 & 0.5263 \end{pmatrix}\begin{pmatrix} 6 \\ 3 \\ -4 \end{pmatrix}=\begin{pmatrix} 7.8 \\ 0.1455 \\ 0.3263 \end{pmatrix}$$

The calculated result means that rolled fcc metal with the (123)[6 3-4] orientation transforms to (-0.1156 3.5441 1.1947)[7.8 0.1455 0.3263] ≈ (-1 31 10)[54 1 2] after Rex. For polycrystalline metals, the {123}<634> deformation texture transforms to the {-0.1156 3.5441 1.1947}<7.8 0.1455 0.3263> ≈ {1 31 10}<54 1 2> Rex texture. The Rex texture is shown in Figure 46a. If the {-0.1156 3.5441 1.1947}<7.8 0.1455 0.3263> orientations are expressed as Gaussian peaks with scattering angle of 10°, the Rex texture is very well approximated by the {310}<001> texture as shown in Figure 46b. This texture is similar to Figure 27 which shows the Rex texture of the plane strain compressed {123}<412> crystal.

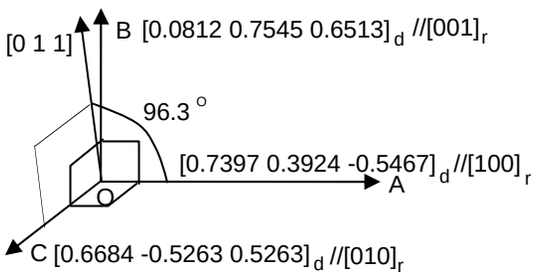

Figure 45. Orientation relationship between deformed and Rexed states [61].

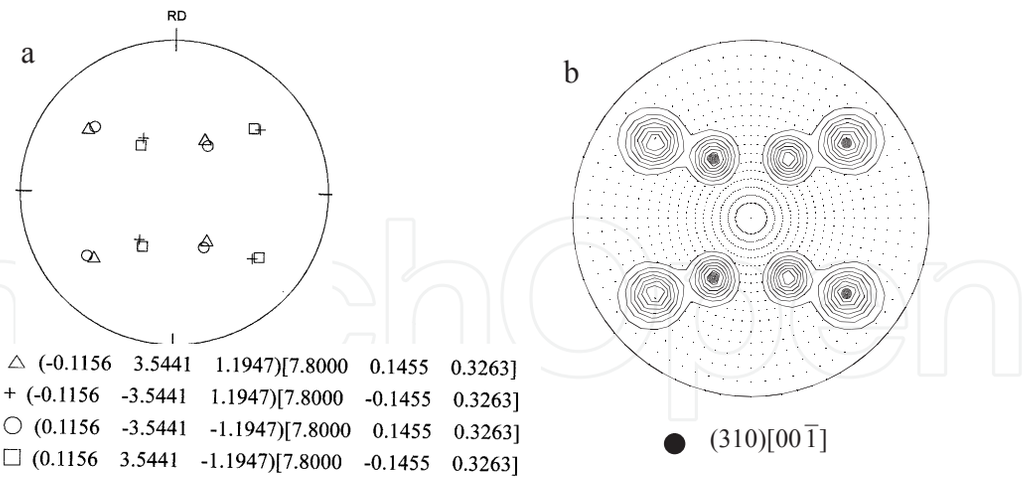

Figure 46. (a) (111) pole figure of {0.1156 3.5441 1.1947}<7.8 0.1455 0.3263> ≈ {1 31 10}<54 1 2>. (b) Sum of {0.1156 3.5441 1.1947}<7.8 0.1455 0.3263> expressed as Gaussian peaks with scattering angle of 10°. Calculated orientation can be approximated by {310}<001> [61].

It is noted that the highest density component in the deformation texture does not always dominate the Rex texture. All the components in the deformation texture are not in equal position to nucleate and grow the corresponding components in the Rex texture. The brass

component has the highest density, but has lowest stored energy or the Taylor factor, while the copper component has the lowest density, but has the highest stored energy or the Taylor factor. If grains with the Goss or cube orientation survived during rolling, they must have undergone plane strain compression. They could undergo recovery and act as nuclei for Rex during annealing. This is the reason why the cube Rex texture could be obtained even though the copper component is the least in the deformation texture. When other conditions are the same, the higher relative density component in the deformation texture will give rise to the higher density in the corresponding component in the Rex texture, as shown in the highest relative copper component in the deformation texture yielding the highest cube component in the Rex texture in the Cu-4%Mn alloy among the three Cu-Mn alloys.

7. Plane-strain compressed {110}<001> bcc steel crystal

The Goss orientation {110}<001> in about 3% Si steel has been the subject of speculation due to its scientific and technological points of view. The grain oriented Si steel is made by hot rolling, cold rolling, followed by annealing. The Goss texture is formed near the sheet surface layer rolled in the α phase region at elevated temperatures. The friction between the sheet and rolls tends to increase with increasing temperature, and in turn increases the shear deformation and the Goss texture (Figure 47).

7.1. Thermal stability of Goss orientation formed by shear deformation

During hot rolling, Rex can take place, thereby the Goss orientation may change to a different orientation. Lee and Lee [64] obtained an IF steel specimen with only the shear texture by a multi- layer warm rolling and discussed the evolution of its Rex texture. The material used was a hot rolled 3.2 mm thick IF steel sheet. The hot-rolled sheet was cold-rolled to 1.1 mm in thickness in several passes. Four of the 1.1mm thick sheet were stacked, heated at 700 ^{o}C for 30 min and rolled by 70% in the ferrite region without lubrication. The rolled specimen was quenched into 25 ^{o}C water. Each layer was separated from the warm rolled sheet. In order to obtain a uniform shear texture, the surface layer was thinned from the inner surface to a half thickness by chemical polishing. The thinned surface and center layers were annealed at 750 ^{o}C for 1 h in Ar atmosphere.

The measured (110) pole figures and ODFs of the outer and inner surfaces of the 75% warm-rolled surface layer were similar. The similarity indicates that the texture of the layer is uniform. The texture was approximated by the Goss orientation plus minor {112}<111>. The center layer was similar to the typical texture of cold rolled steel sheet, RD//<110> and ND//{111}(Section 8). The surface texture could also be described as that which is obtained when the center layer texture is rotated through 35^{o} about TD. The measured textures were similar to the calculated textures in Figure 47. The textures of the chemically thinned rolled surface layer and the center layer after annealing at 750 ^{o}C for 1 h showed that the texture of the surface layer was almost the same before and after annealing while the center layer underwent a

texture change after annealing. Microstructures and hardness tests of the surface layer before and after annealing indicated Rex occurring after annealing [64].

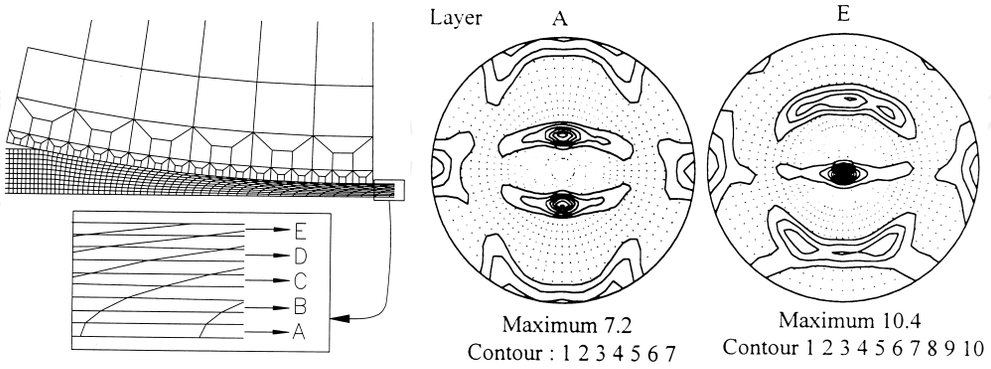

Figure 47. Deformed FEM meshes in rolling and calculated (110) pole figures of layers A and E. In FEM calculation, flow characteristics of IF steel $\sigma = 500\varepsilon^{0.256}$ MPa, roll diameter of 310 mm, initial sheet thickness of 3.4 mm, and reduction of 70% were used [63].

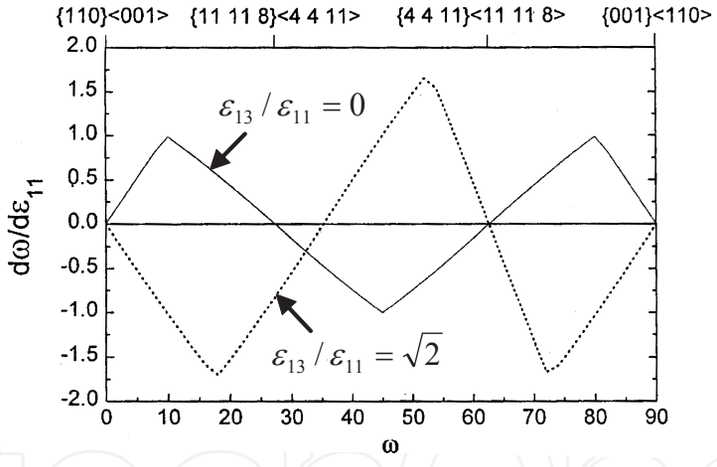

Figure 48. Rotation rate $d\omega/d\varepsilon_{11}$about TD//<110> with respect to ε_{11} for bcc crystal [64].

$d\varepsilon_{13}/d\varepsilon_{11}$	$\gamma^{(1)}$	$\gamma^{(2)}$	$\gamma^{(3)}$	$\gamma^{(4)}$
0.5	1.225	1.225	0.245	0.245
1.0	1.225	1.225	1.120	1.120
1.2	1.225	1.225	1.466	1.466
√2	1.225	1.225	1.837	1.837
1.5	1.225	1.225	1.986	1.986

Table 4. Shear strain on each slip system as a function of $d\varepsilon_{13}/d\varepsilon_{11}$ [64].

The unchanged texture in the surface layer after annealing can be explained based on SERM. AMSD is obtained from the slip systems activated during deformation. On the basis of the Taylor-Bishop-Hill theory, the (110)[001] orientation is calculated to be stable at $\varepsilon_{13}/\varepsilon_{11}=\sqrt{2}$ (Figure 48), and active slip systems for the (110)[001] crystal is calculated to be 1 (0-1 1)[111], 2 (-101)[111], 3 (110)[-111], and 4 (110)[1-1 1]. The shear strain on each slip system calculated as a function of $\varepsilon_{13}/\varepsilon_{11}$ is given in Table 4. The shear strains on slip systems 1 and 2 do not change, but those on slip systems 3 and 4 increase with increasing $\varepsilon_{13}/\varepsilon_{11}$. The slip systems 1 and 2 are effectively equivalent to the (-1-1 2)[111] system, and the slip systems 3 and 4 are equivalent to the (110)[002] system. AMSD may be parallel to $\gamma^{(1,2)}$[111]+$\gamma^{(3,4)}$[002] with $\gamma^{(1,2)}$ and $\gamma^{(3,4)}$ being shear strains on slip systems 1 and 2 and slip systems 3 and 4, respectively. Even though the (110)[001] orientation is stable at $\varepsilon_{13}/\varepsilon_{11}=\sqrt{2}$, in real rolling the $\varepsilon_{13}/\varepsilon_{11}$ value is small in the entrance region, increases very rapidly up to a maximum value just ahead of the neutral point, and then decreases in the exit region. The slip systems having the higher shear strain give dominant contribution to AMSD. As shown in Table 4, slip systems 3 and 4 are likely to give dominant contribution to AMSD. Therefore, AMSD is likely to be parallel to the [001] direction, which is also MYMD. Therefore, the Goss orientation is likely to remain unchanged after annealing in agreement with the experimental result (1st priority in Section 2). Another reason for the thermal stability of shear deformation textures is described in [65].

7.2. Plane-strain compressed {110}<001> bcc metals

The (110)[001] orientation of bcc metals is calculated to be metastable with respect to plane strain compression (Figure 48), with active slip systems being (-1 0-1)[-1-1 1], (1 0-1)[111], (0-1-1)[-1-1 1], and (0 1-1)[111], on which the shear strain rates are the same. It is noted that the slip directions are chosen to be at acute angles with the [001] direction (Section 2). The two slip directions, [-1-1 1] and [111], are on the (-110) plane, which can be a slip plane in bcc crystals. Therefore, AMSD is [-1-1 1] + [111] = [002] // [001]. This is also MYMD of iron. Since the AMSD is the same as MYMD, if the Goss oriented crystal survives the plane-strain compression, the Goss texture is likely to remain unchanged during annealing according to SERM (1st priority in Section 2).

7.3. Evolution of Goss recrystallization texture from {111}<112> rolling texture

The Goss orientation, which is not stable with respect to plane strain deformation, rotates toward the {111}<112> orientation forming a strong maximum [66]. The relaxed constraints Tayor model, in which shear strains parallel to RD may occur, causes the formation of the {111}<112> orientation [67]. The {111}<112> rolling component is known to lead to the Goss orientation after Rex [66, 68]. Dorner et al. [68] attributed the transition from the {111}<112> deformation texture to the Goss Rex texture to the fact that the Taylor factor (2.4) of the Goss grains is lower than that (3.7) of the {111}<112> matrix. Dorner et al. [69], in their study with 3.2% Si-steel single crystals, also found two types of Goss crystal volumes in 89 % cold-rolled specimen. Most of the Goss crystal regions are situated inside of shear bands. The Goss crystal volumes are also observed inside of microbands. These Goss crystals may act as nuclei because they are thermally stable (Section 7.2).

http://dx.doi.org/10.5772/54123

The evolution of the Goss orientation in the (111)[1 1-2] component, a {111}<112>, has been explained by SERM [70]. Slip systems of (-1-1 0)[-1 1-1], (-1-1 0)[1-1-1], (101)[1 1-1], and (011)[1 1-1] are calculated, by the relaxed constraints Taylor model, to be equally active in the (111)[1 1-2] crystal undergoing the plane strain compression. It is noted that the three slip directions are chosen to be at acute angles with RD [1 1-2] of the crystal. Taking the (101)[1 1-1] and (011)[1 1-1] slip systems sharing the same slip direction [1 1-1] into account, AMSD is [-1 1-1] + [1-1-1] + [1 1-1] = [1 1-3]. According to SERM, this AMSD [1 1-3] becomes parallel to MYMD, the <100> directions in bcc iron, in Rexed crystals. Other directional relationships between the matrix and Rexed crystal can be obtained from the 2nd priority in Section 2. Let one of the <100> directions be the [001] direction, then it must be on the (100), (010) or (110) plane, taking the symmetry condition into account. TD of the (111)[1 1-2] crystal is the [1-1 0] direction. These facts give rise to orientation relationship between the deformed and Rexed states (Figure 49). It is noted that the [1-1 0] direction is TD of both the deformed and Rexed states. It follows that the (111)[1 1-2] orientation becomes the (441)[1 1-8] orientation after Rex. The symmetry yields another equivalent orientation, (441)[-1-1 8]. The (110) pole figure of the {441}<118> orientation is shown in Figure 50a along with the Goss orientation {110}<001>. The {441}<118> orientation is deviated from the Goss orientation by 10°. If each {441}<118> orientation is represented by the Gauss type scattering with a half width angle of 12°, the calculated result is as shown in Figure 50b, which is in very good agreement with the measured data in Figure 50c, where the highest intensity poles are the same as those of the Goss orientation, even though it is not real Goss orientation. It is also interesting to note that the rotation angle between (111)[1 1-2] and (441)[1 1-8] about a common pole of [110] is calculated to be 25°and the rotation angle between (111)[1 1-2] and (110)[001] about a common pole of [110] is 35°. Thus the {111}<112> matrix can favor the growth of Goss-oriented crystals or nuclei, which are stable during annealing, if any, or may generate Goss-oriented nuclei, especially in polycrystalline materials.

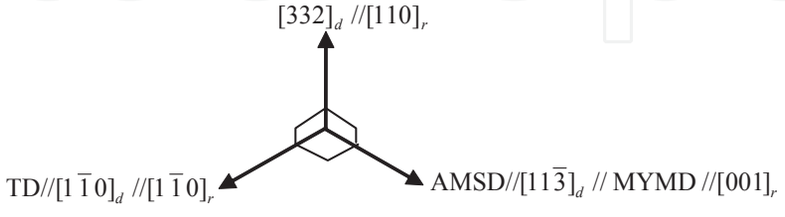

Figure 49. Orientation relationship between deformed ($_d$) and recrystallized ($_r$) states.

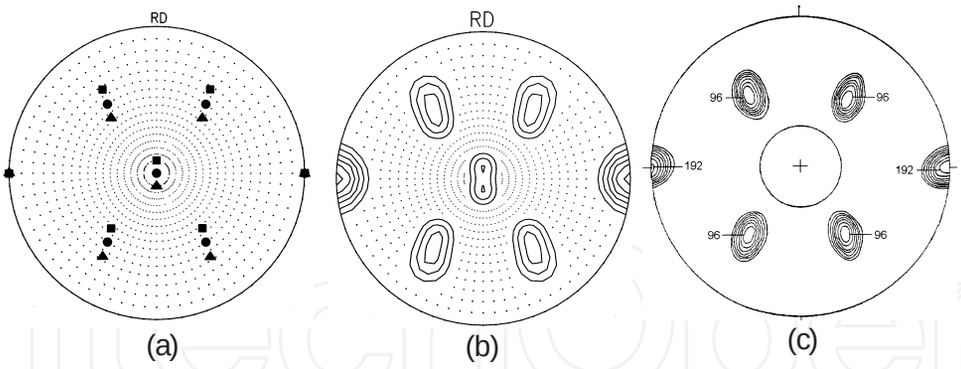

Figure 50. pole figures for (a) {110}<001> and {441}<118> orientations (●(110)[0 0-1], ■(441)[1 1-8], ▲(4 4-1) [-1-1-8]) [70], (b) Gaussian function of {441}<118> with half width of 12° and I_{max}=11 [70], and (c) Si steel specimen Rexed for 1 min at 980 °C [66].

8. Cold-rolled polycrystalline bcc metals

It is well known that the rolling texture of bcc Fe is characterized by the α fiber (<110>//RD) plus the γ-fiber (<111>//ND) and the rolling texture is replaced by the γ-fiber after Rex (Figure 51). This texture transformation will be discussed based on SERM. Figure 52 shows ODFs of 50, 80, and 95% cold-rolled IF steel sheets and their Rex textures, which indicate that the deformation textures are approximated by the α and γ fibers and the Rex texture by the γ fiber, as well known. As the deformation increases, peak type orientations tend to form. For the 80 and 95% cold rolled specimens, the {665}<110>, {558}<110>, and {001}<110> orientations develop as the main components. The {665}<110> and {558}<110> orientations may be approximated by the {111}<110> and {112}<110> orientations, respectively. The {001}<110> component is the principal component inherited from the hot band. It is stable and its intensity increases with deformation [72,73]. The Rex texture is approximated by the γ fiber whose main component is approximated by {111}<112>. The density of this orientation increased with increasing cold rolling reduction.

Figure 53 shows the orientation densities along the α and γ fibers for IF steel rolled by 80% and annealed at 695 °C. Up to 100 s, little change in the orientation density occurs, although appearance of the {111}<112> component in the γ fiber is apparent. For the specimen annealed for 200 s, the orientation density along the γ fiber is almost as high as that of the fully annealed one, while the density along α fiber decreases with increasing annealing time.

8.1. Recrystallization in γ fiber

We want to know if the {111}<112> Rex texture results from the {111}<110> deformation texture. The (111)[1-1 0] orientation is taken as an orientation representing the {111}<110> deformation texture. The (111)[1-1 0] orientation is calculated to be stable using the rate sensitive model

with pancake relaxations (ε_{13} and ε_{23} are relaxed.). The active slip systems of the (111)[1-1 0] crystal are calculated to be (101)[1-1-1], (0-1-1)[1-1 1], (211)[1-1-1], and (-1-2-1)[1-1 1], on which the shear strain rates $d\gamma^{(k)} / d\varepsilon_{11}$ with respect to ε_{11} are 0.0612, 0.0612, 0.107 and 0.107, respectively. It is noted that the slip directions are chosen to be at acute angles with RD. The four slip systems can be effectively divided into the following two slip systems. 0.0612(101)[1-1-1] + 0.107(211)[1-1-1] // (0.2752 0.107 0.1682)[1-1-1] and 0.0612(0-1-1)[1-1 1] + 0.107(-1-2-1)[1-1 1] // (-0.107 -0.2752 -0.1682)[1-1 1]

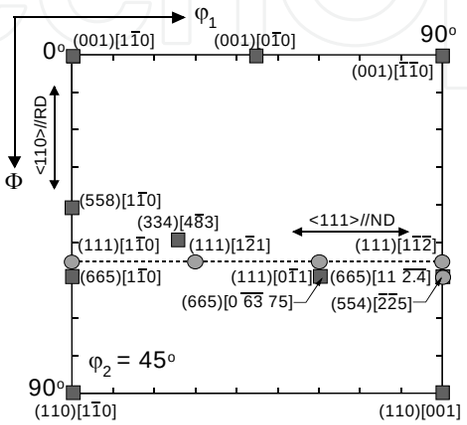

Figure 51. Section of φ_2 =45° in Euler space with locations of important orientations and fibers.

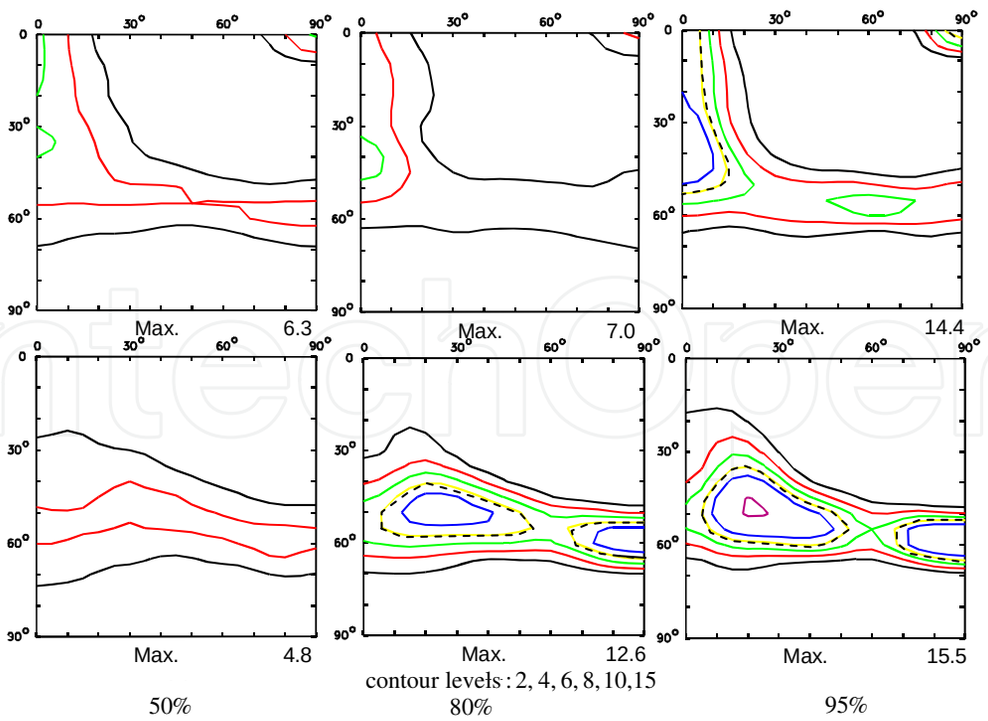

Figure 52. ODFs (φ_2= 45°) of 50, 80, and 95% rolled IF steel sheets (top) before and (bottom) after annealing at 695 °C for 1000 s [71]

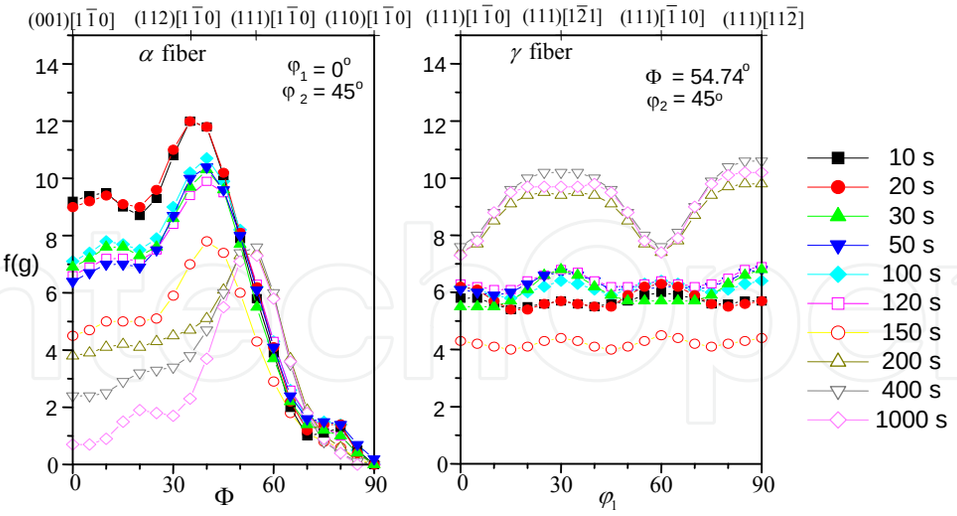

Figure 53. Orientation densities along α and γ fibers for IF steel sheets cold-rolled by 80% and subsequently annealed at 695°C for 10 to 1000 s [71].

These two slip systems are depicted as locating in the opposite sides of the rolling plane as shown in Figure 54a, and they are physically equivalent. They may not be activated homogeneously, even though they are equally activated macroscopically. In this case, AMSD is [1-1-1] or [1-1 1]. It should be mentioned that all active slip directions are not summed unlike fcc metals in which all slip directions are related to each other through associated slip planes. Figure 54b shows angular relationships among MYMD [100], ND [111], and RD [2-1-1] in the (111)[2-1-1] grains, whose orientation has been supposed to be the Rex texture of the (111)[1-1 0] rolling texture. It can be seen that [1-1 1] in Figure 54a is not parallel to [100] in Figure 54b. According to SERM, the {111}<110> rolling texture is not likely to link with the {111}<112> Rex texture.

Examining the experimental results more closely, the evolution of the {665}<1 1 2.4> Rex texture [(φ_1,Φ,φ_2)=(90°,59.4°,45°)] appears to be linked to the {665}<110> deformation texture [(φ_1,Φ,φ_2)=(0°,59.5°,45°) or (54.8°,58.7°,50°)]. Let the (665)[1-1 0] orientation be an ideal orientation representing the {665}<110> deformation texture. The (665)[1-1 0] orientation is calculated to be stable using the rate sensitive slip with pancake relaxations. Calculated active slip systems and their activities in the (665)[1-1 0] crystal are given in Table 5. Active slip directions are [1-1-1], [1-1 1], and [1 1-1]. It is noted that the [1-1-1] and [1-1 1] slip directions are chosen to be at acute angles with RD and physically equivalent. The [1 1-1] direction is normal to RD. The relationship between various directions is shown in Figure 55. AMSD is therefore (0.0536 + 0.0086 + 0.0843)[1-1-1] + (0.0368 + 0.0148 + 0.0148)[-1-1 1] = [0.0801 -0.2129 -0.0801] // [1 -2.658 -1] or (0.0536 + 0.0086 + 0.0843)[1-1 1] + (0.0368 + 0.0148 + 0.0148)[1 1-1] = [0.2129 - 0.0801 0.0801] // [2.658 -1 1]. The second term direction in AMSD is determined physically with reference to Figure 55a. For the first term direction of [1-1 1], the angle between the [1-1 1] direction and TD [-1-1 2.4] direction is less than 90°. Therefore, the angle between the [-1-1 2.4] direction and the second direction, [-1-1 1] or [1 1-1], should be larger than 90° and so the [1 1-1] direction is chosen.

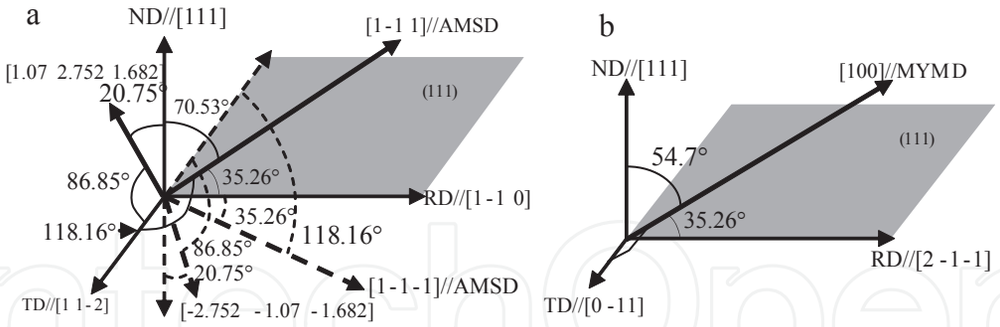

Figure 54. Angular relationships (a) among AMSD, ND, and RD in rolled (111)[1-1 0] crystal and. (b) among MYMD, ND, and RD in (111)[2-1-1] crystal.

Slip direction		1-1-1			1-1 1			1 1-1	
Slip plane	101	211	312	0-1-1	-1-2-1	-1-3-2	112	123	213
$\lvert d\gamma^{(k)}/d\varepsilon_{11}\rvert$, $d\varepsilon_{11}$=0.01	0.0536	0.0086	0.0843	0.0536	0.0086	0.0843	0.0368	0.0148	0.0148

Table 5. Shear strain rates on slip systems in plane strain compressed (665)[1-1 0] crystal calculated based on rate sensitive pancake model [71]

For the (665)[-1-1 2.4] orientation as an orientation representing the {665}<1 1 2.4> Rex texture, the angles among ND, TD, RD, and [001] are shown in Figure 55b. Comparison of Figures 55a and 55b shows that AMSD in the deformed specimen is almost parallel to [001], MYMD of iron, in the Rexed specimen. This is compatible with SERM. In other words, the transformation from the (665)[1-1 0] deformation orientation to the (665)[1-1 2.4] Rex orientation is compatible with SERM. The deformed matrix and Rexed grains share the [665] ND (2nd priority in Section 2). Taking symmetry into account, the {665}<110> rolling texture is calculated to transform to the {665}<1 1 2.4> Rex texture, in agreement with the experimental result. This transformation relationship may be approximated by the transformation from the {111}<110> deformation texture to the {111}<112> Rex texture.

The {111}<112> orientation is not stable with respect to plane-strain compression. However, if the orientation survived during rolling, grains with the orientation must have been plane-strain compressed. The plane-strain compressed (111)[1 1-2] crystal is calculated, by the full constrains model, to have slip systems of (110)[1-1-1] and (110) [-1 1-1], whose activities are the same, if we consider slip systems on one side of the rolling plane. It is noted that the slip directions are at acute angles to RD and on the same slip plane. AMSD is calculated to be [1-1-1] + [-1 1-1] = [0 0-2], which is parallel to a MYMD (Figure 56a). Therefore, the {111}<112> deformation texture is likely to remain unchanged during annealing (1st priority in Section 2). The {111}<112> grains may act as nuclei.

Yoshinaga et al. [74] observed that a {111}<112> nucleation texture was strongly formed in 65% rolled iron electrodeposit with a weak {111}<112> texture, resulting in the {111}<112> Rex

texture, whereas a {111}<110> nucleation texture was formed in 80% rolled electrodeposit having a strong{111}<112> texture, resulting in the {111}<110> Rex texture. They noted the importance of the nucleation texture in the Rex texture formation and attributed to the {111}<110> Rex texturing in the 80% rolled sheet to higher mobility of grain boundaries between the {111}<110> grains and the{111}<112> deformed matrix. They did not account for the differences in nucleation texture between the 65% and 80% rolled sheets.

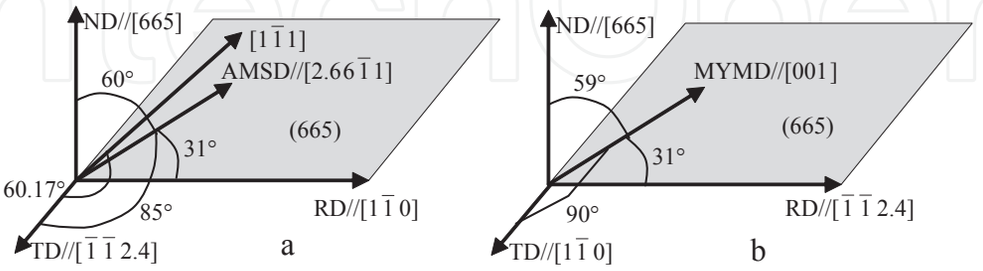

Figure 55. (a) AMSD in (665)[1-1 0] rolled crystal; (b) MYMD in (665)[-1-1 2.4] Rexed crystal [71].

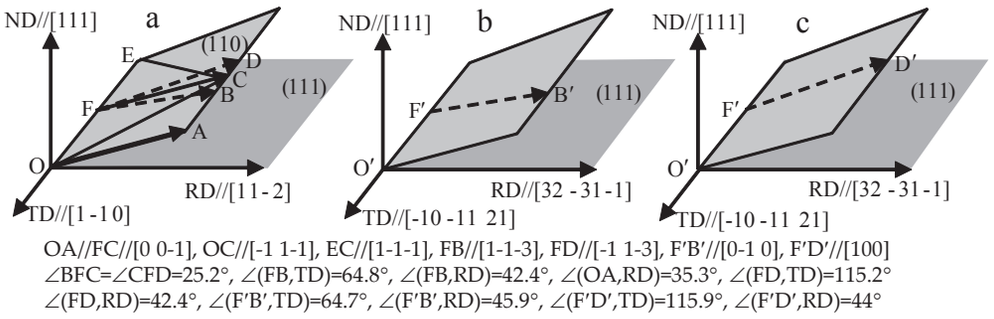

Figure 56. Explanation of {111}<112> rolling texture changing to {111}<112> or {111}<110> after Rex. F′B′ and F′D′ are MYMDs in Rexed state and are almost parallel to AMSDs, FB and FD, in deformed state, respectively [5].

According to SERM, the {111}<112> deformation texture is likely to remain unchanged after Rex because AMSD in the deformed state is parallel to MYMD, as mentioned above. If the activities of the slip systems of (110)[-1 1-1] and (110)[1-1-1] in Figure 56a are well balanced, MYMD becomes [0 0-1]. This may be the case in the 65% rolled sheet. As the rolling reduction increases, the balance can be broken. When the (110)[1-1-1] slip system is two times more active than the (110)[-1 1-1] system, AMSD is parallel to the [1-1-3] direction (2[1-1-1] + [-1 1-1] = [1-1 -3]). Similarly if the (110)[-1 1-1] system is two times more active than the (110)[1-1-1] slip system, AMSD is parallel to the [-1 1-3] direction. These directions are shown in Figure 56a. If one of the two slips takes place in one layer and another one does in another layer and so on, as in ε_{23} relaxation, the rolling texture macroscopically appears the same as in the balanced slip. When these AMSDs are made to be parallel to MYMD, one of the <100> directions, as shown in Figures 56b and 56c, we come to the result that the {111}<112> rolling texture is linked with the {111}<32 31 1> Rex texture that is approximated by the {111}<110> texture.

As the Rexed {665}<1 1 2.4> and {111}<112> grains grow, they are likely to meet the α fiber grains. If the Rexed grains are not in a favorable orientation relationship with the α fiber grains, they may not grow at the expense of the α fiber grains. This is discussed in the next section.

8.2. Recrystallization in α fiber grains

Park et al. [75,76] discussed orientation relationships between the rolling and Rex textures in rolled IF steel sheets based on both SERM and the conventional OG, in which the α-fiber rolling texture was assumed to transform to the γ-fiber Rex texture. The {001}<110> and {112}<110>rolling orientations, which are main components in the α-fiber texture, are calculated to be stable using the full constraints Taylor model. For the (001)[110] orientation as an orientation representing the {001}<110> orientation, active slip systems are calculated to be (1 1-2)[111] and (112)[1 1-1] from the full constraints Taylor model. Therefore, AMSD can be [111] or [1 1-1]. Figure 57a shows the angular relation between the [111] direction and the (001)[110] specimen axes. Figure 57b shows the angular relation between the [001] direction, which is a MYMD, and the axes of the specimen with the (111)[-1-1 2] Rex texture. It can be seen from Figure 57 that AMSD in the deformed state is parallel to MYMD in the Rexed state and TD is shared by the deformed and Rexed states (2nd priority in Section 2). Taking the symmetry into account, the {001}<110> deformation texture is calculated to transform into the {111}<112> Rex texture. This transformation was observed in the experimental results (Figures 52 and 53, [75], [77]). It is often addressed that the {001}<110> orientation is difficult to be Rexed. It may be attributed to the fact that the orientation has a low Taylor factor [66].

For the (558)[1-1 0] orientation as an orientation representing the {558}<110> orientation, active slip systems are calculated to be 2.283(101)[1-1-1], (101)[-1-1 1], 2.283(0-1-1)[1-1 1], and (0-1-1)[1 1-1] from the full constraints Taylor model, where the factor 2.283 in front of slip systems indicates that their activities are 2.283 times higher than other slip systems [66]. The slip systems reduce effectively to (101)[1-2.56-1] and (0-1-1)[2.56-1 1]. Therefore, AMSD becomes [1-2.56-1] or [2.56 -1 1]. Figure 58 shows that the [1-2.56-1] direction in the (558)[1-10] crystal is nearly parallel to MYMD in the Rexed state, and the [101] direction is shared by the deformed and Rexed states (2nd priority in Section 2). Taking the symmetry into account, the {558}<110> deformation texture is calculated to transform into the {334}<483> Rex texture. This transformation relation was observed in the experimental result. The {334}<483> orientation is away from the {111}<112> orientation. An exact correspondence between the (112)[-110] deformation and (-2.45 2 –2.45)[1 2.45 1] Rex orientations can be seen in Figure 59.

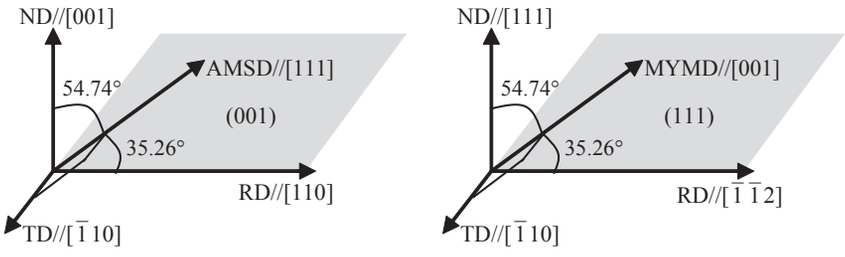

Figure 57. AMSD in (001)[110] rolled crystal and MYMD in (111)[-1-1 2] Rexed crystal [71].

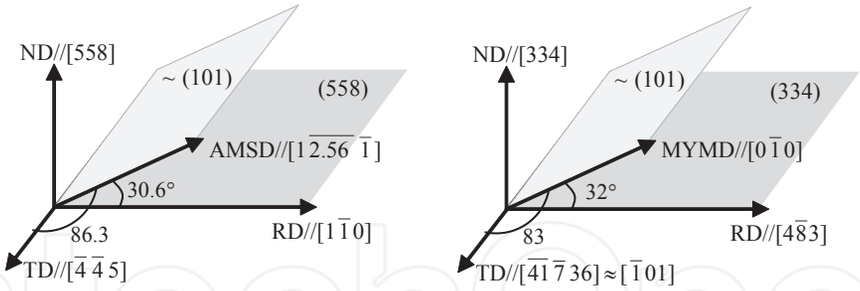

Figure 58. AMSD in (558)[1-1 0] rolled crystal and MYMD in (334)[4-8 3] Rexed crystal [71].

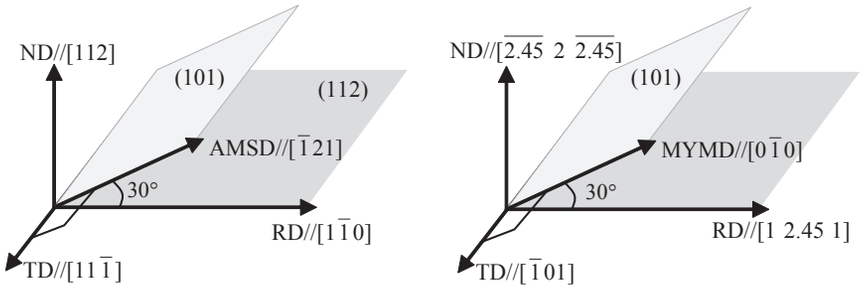

Figure 59. AMSD in (112)[-110] rolled crystal and MYMD in (-2.45 2 -2.45)[1 2.45 1] Rexed crystal [71].

Park et al. [75] studied relationships between rolling and Rex textures of IF steel. When the {112}<110>, {225}<110>, and {112}<110> components had the highest density in cold rolling texture, the {567}<943>, {223}<472>, and {554}<225> components had the highest density in Rex texture, respectively. Rolling and Rex textures of low carbon steel (C in solution), and Fe-16%Cr and Fe-3%Si steels indicate that the strong rolling texture components {001}<110> and {112}<110> have an effect on the evolution of a very strong Rex texture {111}<112> [77].

Park et al. [76] investigated the macrotexture changes in 75% cold-rolled IF steel with annealing time at 650ºC along the α-fiber. The cold rolling texture showed the development of the α fiber as typical in bcc steels. The orientation densities of the α-fiber increased slightly after annealing for 300 s. This is a well-known recovery phenomenon. A part of the α-fiber, near {114}<110>, substantially decreased after annealing for 1000 s. EBSD analysis indicated that the {556}<175> Rex component was formed at the expense of the {114}<110> deformation component. This texture transformation could be explained by SERM. Relationships between various rolling and Rex textures are summarized in Table 6.

These results can be explained based on SERM [4,75,76]. Figure 60 shows drawings relating the rolling texture components to the Rex texture components. AMSDs can be easily obtained by choosing the <111> directions, the slip directions in bcc metals, closest to 45º to the compression axis without calculation of rolling deformation. For the cold rolling texture (001)[110], TD is calculated by the vector product of [110] and [001] to be [-110]. The <111> directions closest to 45º with the [001] compression axis are [-111], [-1-1 1], and [111]. The [-111] direction is likely to contribute to spread of the width of sheets. Therefore, slip along the [-111] direction is unlikely. The effective slip planes are likely to be parallel to TD and contain the [111] and [-1-1 1] slip directions. The planes are those normal to the vector product of the [-110] TD and the [-1-1 1] and/or

[111] directions. They are calculated to be the (112) and/or (1 1-2) planes. The related slip systems are therefore (112)[-1-1 1] and (1 1-2)[111]. These systems are physically equivalent. Therefore, it is sufficient to choose one of them. Let us choose the [111] direction. The [111] direction and other related directions and planes are shown in Figure 60a. The [111] direction is on ND-RD plane. Therefore, it is likely to be AMSD.

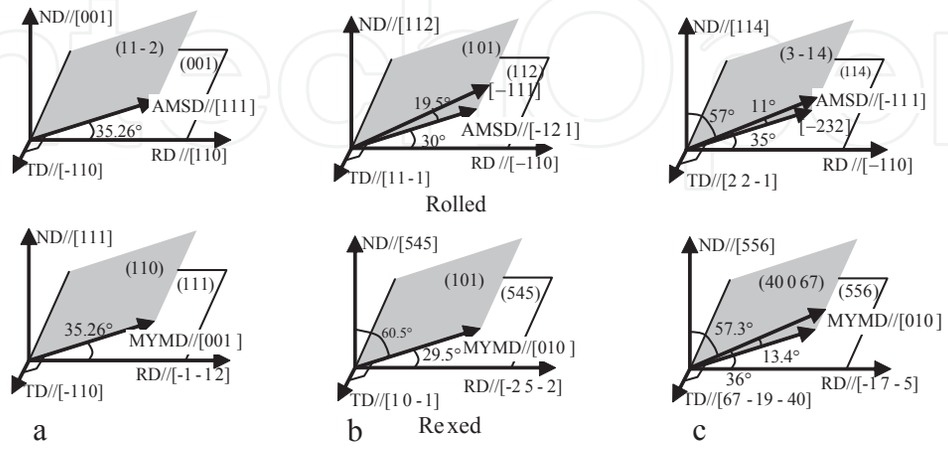

Figure 60. Correspondence between AMSD in rolled state (top), MYMD in Rexed state (bottom) in orientation relationships between (a) (001)[110] roll ↔ (111)[-1-1 2] Rex, (b) (112)[-110] roll ↔ (545)[-2 5-2] Rex, (c) (114)[-110] roll ↔ (556)[-1 7-5] Rex.

If the [111] direction in the deformed state is set to be parallel to MYMD [001] in the Rexed state, the (111) plane becomes parallel to the rolling plane and the [-1-1 2] direction becomes parallel to RD in the Rexed state, giving rise to the (111)[-1-1 2] Rex texture as shown in Figure 60a. This result is the same as that obtained based on the full-constraints Taylor model (Figure 57). Therefore, the {001}<110> may be responsible for the measured {111}<112> Rex texture. It is noted that the [-110] TD is shared by both the deformed and Rexed states (2nd priority in Section 2). It is also noted that the angle between AMSD and RD is about 30° which is the usually observed angle between the shear band and RD.

Other examples in Figure 60 are self-explainable. In all the examples except Figure 60d, the <110> directions are shared by the deformed and Rexed states. In fact, the Rex textures in Figure 60b and 60c are very similar. This is the reason why there exists an angular relation between the deformed and Rexed states about the <110> axes (Table 6). This has often been interpreted to be associated with CSL boundaries. However, there is no consistency in the CSL boundaries. Anyhow the high density orientations along the α fiber change to near {111}<112> orientations on Rex.

As the Rexed γ fiber grains grow, they are likely to meet the α fiber grains. Main components in α fiber including the {112}<110> orientation are predicted to tend to change to near {111}<112> orientations according to SERM. Therefore, the {111}<112> Rexed grains will grow at the expense of the α fiber grains with little disturbance of orientation. It is interesting to note that SERM can satisfy the relation between the deformation and Rex textures in the nucleation and growth stages. The two prominent components, (334)[4-8 3] and (554)[-2-2 5], in the Rex texture are related to the (558)[1-1 0] and (112)[1-1 0] components in the rolling texture, respectively.

Rolling texture Component	Rex texure Component	RD↔AMSD (°)	RD↔MYMD (°)	Observed OR	Coincidence site lattice relation
{112}<110>	{567}<943>	30	29	30°<110>	Σ19a(26.5°<110>)
{225}<110>	{223}<472>	35.3	32.6	25°<110>	Σ19a(26.5°<110>)
{112}<110>	{554}<225>	30	29.5	35°<110>	Σ9(38.9°<110>)
{001}<110>	{111}<112>	35.3	35.3	55°<110>	Σ11(50.5°<110>)
{114}<110>	{556}<175>	35	36		
{558}<110>	{334}<483>	30.6	32	29°<110>	Σ19a (26.5°<110>

Table 6. Orientation relationships (OR) between major components which dominate rolling and Rex textures.

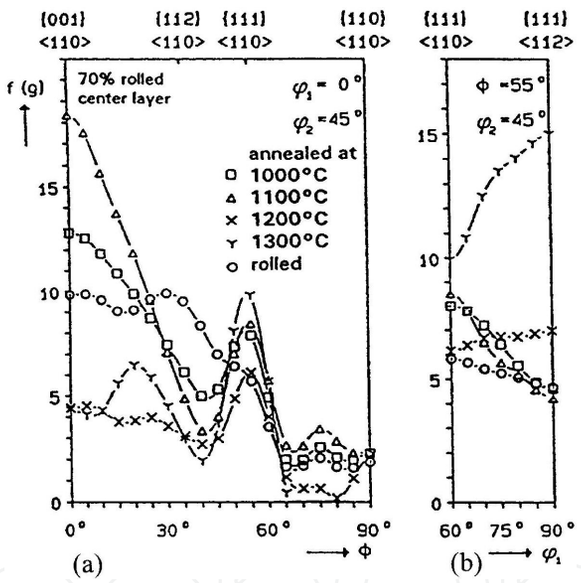

Figure 61. Orientation densities along α- and β- fibers for 70% rolled and annealed Ta [78].

8.3. Recrystallization in non-ferrous bcc metals

The texture evolution in Ta after 70% rolling and subsequent annealing at various temperatures is shown in Figure 61 [78]. The rolling texture of Ta is characterized by a partial α-fiber extending from {001}<110> to {111}<110> and a complete γ-fiber {111}<uvw>. The major deformation texture components are {112}<110> and {001}<110> as in steel. MYMD of Ta is <100> (A>0 in Table 6), the development of the Rex texture is expected to be similar to that in steel. It can be seen that an enhancement of {001}<110> due to recovery and a strong decrease

in {001}<110> to {112}<110> accompanied by a strong increase in γ-fiber {111}<112> and/or {554}<225> due to Rex. The Rex behavior is readily understood from Figure 60 [4, 75].

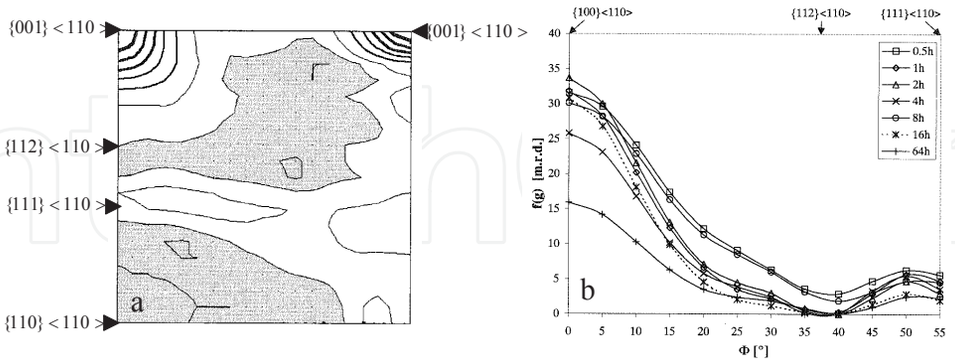

Figure 62. (a) φ_2 =45° ODF section of center of Mo sheet annealed for 1h at 925°C and (b) orientation density along α-fiber in central zone of Mo sheet annealed at 850°C [79].

The deformation texture of rolled Mo sheets was characterized by a weak γ-fiber and α-fiber with a strong {100}<110> component [79]. Full Rex does not change the rolling texture but reduces its intensity (Figure 62). This result is compatible with SERM considering that the <111> directions are not only slip directions, which is approximately AMSD (Figure 60a, top), but also MYMD of Mo (A<0 in Table 7) (1st priority in Section 2). The decrease in orientation density during annealing may be attributed to A being close to unity.

Since the slip systems of W are {112}<111> [80], it is predicted that the {001}<110> component dominates the rolling texture as shown in Figure 60a. Figure 63a shows the rolling texture which is dominated by the {100}<011> component as predicted. The deformation texture is approximately randomized after Rex (Figure 63b). This is compatible with SERM because W is almost isotropic in its elastic properties (A≈1 in Table 7).

Material	Temp., K	f S_{11}	f S_{44}	f S_{12}	A	Reference
Ta	1300	8.137	13.966	-3.150	1.6164	82
	1400	8.297	14.025	-3.224	1.6429	
	1500	8.408	14.184	-3.274	1.6472	
	1600	8.576	14.409	-3.357	1.6563	
Mo	273	2.607	9.158	-0.622	0.7052	83
	373	2.655	9.242	-0.682	0.7092	
	973	3.010	9.823	-0.833	0.7824	
W	100	2.398	6.158	-0.665	0.9948	84
	297	2.454	6.218	-0.690	1.0113	85
	973	2.711	6.553	-0.798	1.0710	85
	2073	3.509	7.375	-1.160	1.2662	85

Table 7. S_{ij} (GPa^{-1}) and A=2(S_{11}-S_{12})/S_{44} for Ta, Mo, and W. f =1000

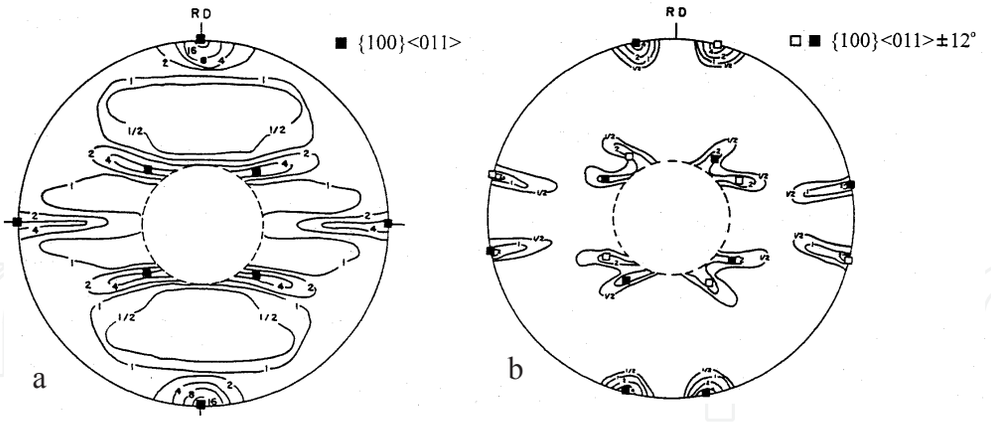

Figure 63. Pole figure of W sheet (a) after cold rolling by 96% and (b) subsequent annealing at 2000 °C for 30 min [81]. Max intensity: (a) >16 and (b) >4. Contour levels: 1/2, 1, 2, 4, 8, 16.

9. Conclusion

The Rex textures of freestanding electro- and vapor-deposits of metals and heavily deformed metals and alloys whose stored energies due to dislocations constitute the main driving forces for Rex can be determined such that AMSDs in the fabricated matrix can be along MYMDs in Rexed grains or nuclei, and by other conditions which can maximize the strain-energy release in the system. The strain-energy-release-maximization theory can explain the following results.

1. The <100>, <111> and <110> electro- and vapor-deposition textures of Cu, Ni, and Ag transform to the <100>, <100>, and <√3 1 0> textures, respectively, after Rex.
2. The <100> and <111> deposition textures of Cr remain unchanged after Rex.
3. The <111>+<100> drawing textures of uniaxially drawn Ag, Al, Cu, and Au wires change to the <100>textures after Rex.
4. Channel-die compressed {110}<001> Al single crystal keeps its {110}<001>deformation texture after Rex.
5. The {135}<2 1-1> Al sheet obtained by channel-die compression of Al crystals of {123}<412> orientations by 90% develops {-0.0062 0.2781 0.9606}<0.9907 0.1322 -0.0319> ≈ {0 1 3.5}<31 4 -1> after Rex.
6. An Al crystal of {112}<111> obtained by channel-die compression of a (001)[110] Al single crystal develops {001}<√610> after Rex.
7. The (123)[-6-3 4] + (321)[-436] + {112}<111> Cu sheet obtained after reversible rolling of a (123)[-6-3 4] Cu single crystal by 99.5% under oil lubrication develops the Rex texture of major {001} <100> + minor (0 3-1)[100] orientations. The {001}<100> and (0 3-1)[100]

components are calculated to result from the {112}<111> and (123)[-6-3 4] components in the deformation textures, respectively.

8. The {011}<211>, {112}<111>, and {123}<634> components in the rolling texture of cold-rolled polycrystalline fcc metals and alloys with medium to high stacking fault energy are respectively linked with the {011}<100>, {100}<001>, and {031}<100> component in the Rex texture.

9. The {111}<112> bcc crystal undergoing plane strain rolling can develop three different Rex textures of {441}<118>≈ {110}<001>, {111}<112>, and ~{111}<110> depending on local slip systems and their activities in the same gloval deformation.

10. The {665}<110>, {001}<110>, {558}<110>, {112}<110>, {114}<110> components in the rolling texture of steel are respectively linked with the {665}<1 1 2.4>, {111}<112>, {334}<483>, {545}<252>, {556}<175> components in the Rex texture.

11. The rolling and Rex textures of Ta are similar to those of steel.

12. Full Rex of Mo does not change the rolling texture but reduces its intensity.

13. The rolling texture of W transforms to a texure which can be approximated by random orientation distribution after Rex.

Acknowledgements

This study was supported by a grant (0592-20120019) from POSCO and a grant(0417-20110114) from Center for Iron & Steel Research of RIAM in Seoul National University.

Author details

Dong Nyung Lee and Heung Nam Han

Department of Materials Science and Engineering, Seoul National University, Seoul, Republic of Korea

References

[1] Burgers WG, Louwerse PC. Über den Zusammenhang zwischen Deformationsvorgang und Rekristallisationstextur bei Aluminium. Zeitschrift für Physik 1931; 61 605-678.

[2] Barrett CS. Recrystallization texture in aluminum after compression. Trans AIME 1940; 137 128-145.

[3] Gottstein G. Evolution of recrystallization texture- classical approaches and recent advances. Materials Science Forum 2002; 408-412 1-24.

[4] Lee DN. The evolution of recrystallization textures from deformation textures. Scripta Metallurgica et Materialia 1995;32 1689-1694.

[5] Lee DN. Relationship between deformation and recrystallization textures. Philosophical Magazine 2005;85 297-322.

[6] Lee DN. Currrent understanding of annealing texture evolution in thin films and interconnects. Zeitschrift für Metallkunde 2005;96 259-268.

[7] Lee DN. Recrystallization-texture theories in light of strain-energy-release-maximization. Materials Science Forum 2010;638-642 182-189.

[8] Lee DN. Strain energy release maximization model for evolution of recrystallization textures. International Journal of Mechanical Sciences 2000;42 1645-1678.

[9] Zehetbauer M. Cold work hardening in stages IV and V of F.C.C. metals—II. Model fits and physical results. Acta Metallurgica et Materialia 1993;41 589-599.

[10] Lee DN. A stability criterion for deformation and deposition textures of metals during annealing. Journal of Materials Processing Technology 2001;117 307-310.

[11] Lee DN. Maximum energy release theory for recrystallization textures. Metals and Materials 1996; 2 121-131.

[12] Lee Y-S, Lee DN. Characterization of dislocations in copper electrodeposits. Journal of Materials Science 2000;35 6161-6168.

[13] Lee DN, Kang S, Yang J. Relationship between initial and recrystallization textures of copper electrodeposits.Plating and Surface Finishing 1995;82(3) 76-79.

[14] Choi J-H, Kang S, Lee DN. Relationship between deposition and recrystallization textures of copper and chromium electrodeposits. Journal of Materials Science 2000;35 4055-4066.

[15] Yang JS, Lee DN. The deposition and recrystallization textures of copper electrodeposits obtained from a copper cyanide bath. Metals and Materials 1999;5 465-470.

[16] Lee DN, Han HN. Orientation relationship between precipitates and their parent phases in steels at low transformation temperatures. Journal of Solid Mechanics and Materials Engineering 2012;6(5) 323-338.

[17] Chang YA, Himmel L. Temperature dependence of the elastic constants of Cu, Ag, and Au above room temperature. Journal of Applied Physics 1966;37 3567-3572.

[18] Kang SY, Lee DN. Recrstallization texture of a copper electrdeposit with the <111> and <110> duplex orientation. Materials Science Forum 2002;408-412 895-900.

[19] Lee DN, Kim YK. In: Kanematsu H. (ed) Variations of texture, surface morphology and mechanical property of copper foils with electrolysis conditions. Proceedings of the 2nd

Asian Metal Finishing Forum, 1-3 June 1985, Tokyo, Japan: The Metal Finishing Society of Japan; 1985. pp. 130-133.

[20] Alers GA, Karbon JA. Elastic moduli of the lead-thallium alloys. Journal of Applied Physics 1966;37 4252-4255.

[21] Kim I, Lee SK. Initial and recrystallization textures of Ni electrodeposits. Textures and Microstructures 2000;34 159-169.

[22] Nam H-S, Lee DN. Recrystallization textures of silver electrodeposits. Journal of the Electrochemical Society 1999;146 (9), 3300-3308.

[23] Bolef DI, de Klerk J. Anomalies in the elastic constants and thermal expansion of chromium single crystals. Physical Review 1963;129 1063-1067.

[24] Patten JW, McClanahan ED, Johnston JW. Room-temperature recrystallization in thick bias-sputtered copper deposits. Journal of Applied Physics 1971;42(11) 4371-4377.

[25] Greiser J, Mullner P, Arzt E. Abnormal growth of giant grains in silver thin films. Acta materialia 2001;49 1041-1050.

[26] Lee DN. Textures and microstructures of vapor deposits. Journal of Materials Science 1999;34 2575-2582.

[27] Carel R, Thompson CV, Frost HJ. Computer simulation of strain energy effects vs surface and interface energy effects on grain growth in thin films. Acta materialia 1996;44 2479-2494.

[28] Lee DN. Texture development in thin films. Materials Science Forum 2002;408-412 75-94.

[29] Hibbard Jr WR. Deformation texture of drawn face centered cubic metal wires. Transactions of AIME 1950;77 581-585

[30] Inoue H, Nakazu N, Yamamoto H. Development of recrystallization texture in drawn aluminum wire. In: Nagashima S. (ed) Proceedings ICOTOM 6, 28 September-3 October 1981, Tokyo, Japan: The Iron and Steel Institute of Japan; 1981. P. 591.

[31] Park H, Lee DN. Effects of shear strain and drawing pass on the texture development in copper wire. Materials Science Forum 2002;408-412 637-642.

[32] Shin HJ, Jeong H-T, Lee DN. Deformation and annealing textures of silver wire. Materials Science and Engineering 2000;A279 244-253.

[33] Ahlborn H, Wassermann G. Einfluss von Verformungsgrad und Temperatur auf die Textur von Silberdrahten. Zeitschrift für Metallkunde 1963;54 1-6.

[34] Lee DN, Chung YH, Shin MC. Preferred orientation in extruded aluminum alloy rod. Scripta Metallurgica 1983;17 339-343.

[35] Park H, Lee DN. The evolution of annealing textures in 90 pct drawn copper wire, Metallurgical and Materials Transactions 2003;34A 531-541.

[36] Cho J-H, Cho J-S, Moon J-T, Lee J, Cho YH, Kim YW, Rollett AD, Oh KH. Recrystallization and grain growth of cold-drawn gold bonding wire. Metallurgical and Materials Transactions A 2003;34A 1113-1125.

[37] Ferry M, Humphreys FJ. Discontinuous subgrain growth in deformed and annealed {110}<001> aluminium single crystals. Acta Materialia 1996;44 1293-1308.

[38] Lee DN. A stability criterion for deformation and deposition textures of metals during annealing. Journal of Materials Processing Technology 2001;117 307-310.

[39] Sutton PM. The Variation of the elastic constants of crystalline aluminum with temperature between 63°K and 773°K. Physical Review 1953;91 816-821.

[40] Blicharski M, Liu J, Hu H. Annealing of aluminum bicrystals with S orientations deformed by channel die compression. Acta Materialia 1995;43 3125-3138.

[41] Lee DN, Jeong H-T. Recrystallization textures of aluminum bycrystals with S orieintation deformed by channel die compression. Materials Science and Engineering 1999;A269 49-58

[42] Butler Jr JF, Blickarski M, Hu H. The formation of dislocation structure and nucleation of recrystallized grains in an aluminum single crystal.Textures and Microstructures 1991;14-18 611-616.

[43] Lee DN (1996). Recrystallization texture of plane strain compressed aluminum single crystal. Texturures and Microstructures 1996;26-37 361-367

[44] Kamijo T, Fujiwara A, Yoneda Y, Fukutomi H. Formation of cube texture in copper single crystals.Acta Metallurgica and Materialia 1991;39 1947-1952.

[45] Lee DN, Shin H-J. Recrystallization texture of (123)[-6-3 4] copper single crystal cold rolled copper sheet. Materials Science Forum 2003;426-432 83-90.

[46] Necker CT, Doherty RD, Rollett AD. Quantitative measurement of the development of recrystallization texture in OFE copper. Textures and Microstructures 1991:14-18 635-640.

[47] Engler O. Recrystallization textures in copper-manganese alloys. Acta Materialia 2001;49 1237-1247.

[48] Koizumi M, Saitou T, Inagaki H. Effect of Mg content of the development of rolling and recrystallization textures in Al-Mg alloys. In Szpunar JA. (ed.) Proceedings of the Twelfth International Conference on Textures of Materials Vol.2, 848-853, Montreal, 9-13 August 1999, Ottawa: NRC Research Press; 1999.

[49] Huh MY, Cho YS, Engler O. Effect of lubrication on the evolution of microstructure and texture during rolling and recrystallization of copper. Materials Science and Engineering 1998;A247 152-164.

[50] Ryu JH, Lee DN. The effect of precipitation on the evolution of recrystallization texture in AA8011 aluminum alloy sheet. Materials Science and Engineering 2002;A336 225-232.

[51] Caleyo F, Baudin T, Penelle R, Venegas V. EBSD study the development of cube recrystallization texture in Fe-50%Ni. Scripta Materialia 2001;45 413-420.

[52] Lee DN, Hong S-H. (2001). Recrystallization textures of plane strain rolled polycrystalline aluminum alloys and copper, In: Recrystallization and Grain Growth, G. Gottstein, D.A. Molodov, (Ed.), 1349-1354, Springer, Berlin.

[53] Godfrey A, Juul Jensen D, Hansen N. Measurement of orientation dependent stored energy of deformation on a local scale. In Gottstein G, Molodov DA (eds.) Recrystallization and Grain Growth, Aachen, 27-31 August 2001, Springer, Berlin, pp843-848.

[54] Hong S-H, Lee DN (2003). The evolution of the cube recrystallization texture in cold rolled copper sheets. Materials Science and Engineering 2003;A351 133-147.

[55] Bauer RE, Mecking H, Lücke K. Textures of copper single crystals after rolling at room temperature. Materials Science and Engineering 1977;27 163-180.

[56] Honeff H, Mecking H. A method for the determination of the active slip systems and orientation changes during single crystal deformation. In: Gottstein G, Lücke K. (eds.) Textures of Materials Vol. 1: proceedings of ICOTOM5, Aachen, Springer-Verlag, Berlin; 1978. P.265.

[57] Van Houtte P. Adaptation of the Taylor theory to the typical substructure of some cold rolled fcc metals. In: Nagashima S. (ed.) Textures of Materials Vol. 1: proceedings of ICOTOM6, The Iron and Steel Institute of Japan, Tokyo; 1981. p. 248.

[58] Steffens T, Schwink C, Korner A, Karnthaler HP. Transmission electron microscopy sudy of the stacking-fault energy and dislocation structure in copper-manganese alloys. Philosophical Magazine 1987;A56(2) 161-173.

[59] Engler O. Deformation and Texture of copper-manganese alloys. Acta materialia 2000;48 4827-4840.

[60] Engler O. Recrystallization textures in copper-manganese alloys. Acta materialia 2001;49 1237-1247.

[61] Lee DN, Shin H-J, Hong S-H. The evolution of the cube, rotated cube and Goss recrystallization textures in rolled copper and Cu-Mn alloys. Key Engineering Materials 2003;233-236 515-520.

[62] Gottstein G. Physicalische Grundlagen der Materialkunde, Springer-Verlag; 1998.

[63] Lee DN, Jeong H-T. The evolution of the goss texture in silicon steel. In: Imam AM, DeNale R, Hanada S, Zhong Z, Lee DN. (eds.) Advanced Materials and Processing: proceedings of the third pacific rim international conference on advanced materials and processing, 12-16 July 1998, Hawaii, Pennsylvania: TMS; 1998.

[64] Lee SH, Lee DN. Shear rolling and recrystallization textures of interstitial-free steel sheet. Materials Science and Engineering 1998;A249 84-90.

[65] Lee DN, Kim K-H. Effects of asymmetric rolling parameters on texture development in aluminum sheets. In: Demer MY. (ed.) Innovations in Processing and Manufacturing of Sheet Materials: proceedings of the second gloval symposium on innovation in materials processing and manufacturing: sheet materials, 11-15 February 2001, New Orleans, Louisiana. Pennsylvania: TMS; 2001.

[66] Dunn CG. Cold-rolled and primary recrystallization textures in cold-rolled single crystals of silicon iron. Acta Metallurgica 1954;2 173-183.

[67] Raabe D, Lücke K. Rolling and annealing textures of bcc metals. Materials Science Forum 1994;157-162 597-610.

[68] Dorner D, Lahn L, Zaefferer S. Investigation of the primary recrystallization microstructure of cold rolled and annealed Fe 3% Si single crystals with Goss orientation, Materials Science Forum 2004;467-470 129-134.

[69] Dorner D, Lahn L, Zaefferer S. Survival of Goss grains during cold rolling of a silicon steel single crystal. Materials Science Forum 2005;495-497 1061-1066.

[70] Lee DN, Jeong H-T. The evolution of the Goss texture in silicon steel. Scripta Materialia 1998;38 1219-1223.

[71] Hong S-H, Lee DN. Recrystallization textures in cold-rolled Ti bearing IF steel sheets. ISIJ International 2002;42 1278-1287.

[72] Seidal L, Hölscher M, Lücke K. Rolling and recrystallization textures in iron–3% silicon. Textures and Microstructures 1989;11 171-185.

[73] Von Schlippernbach U, Emren F, Lücke K. Investigation of the development of the cold rolling texture in deep drawing steels by ODF-analysis. Acta metallurgica 1986;34 1289-1301.

[74] Yoshinaga N, Vanderschueren D, Kestens L, Ushioda K, Dilewijns J. Cold-rolling and recrystallization texture formation in electro-deposited pure iron with a sharp and homogeneous gamma-fiber. ISIJ International 1998;38 610-616.

[75] Park YB, Lee DN, Gottstein G. Evolution of recrystallization textures from cold rolling textures in interstitial free steel. Materials Science and Technology 1997;13 289-298.

[76] Park YB, Lee DN, Gottstein G. The evolution of recrystallization textures in body centered cubic metals. Acta Materialia 1998;46 3371-3379.

[77] Lücke K, Holscher M. Rolling and recrystallization textures of BCC steels. Textures and Microstructures 1991;14-18 585-596.

[78] Raabe D, Lücke K. Rolling and annealing textures of bcc metals. Materials Science Forum 1994;157-162 597-610.

[79] Hünsche I, Oertel C-G, Tamm R, Skrotzki W, Knabl W. Microstructure and texture development during recrystallization of rolled molybdenum sheets. Materials Science Forum 2004;467-470 495-500.

[80] Wassermann G, Grewen J. Texturen metallischer Werkstoffe. Berlin: Springer-Verlag; 1962.

[81] Pugh JW. The temperature dependence of preferred orientations in rolled tungsten.Transactions AIME 1958;212 637.

[82] Walker E, Bujard P. Anomalous temperature behavior of the shear elastic constant c 44 in tantalum. Solid State Communications 1980;34 691-693.

[83] Dickinson JM, Armstrong PE. Temperature Dependence of the Elastic Constants of Molybdenum. Journal of applied Physics 1967;38 602-606.

[84] Bolef DI, de Klerk J. Elastic Constants of Single-Crystal Mo and W between 77° and 500°K. Journal of applied Physics 1962;33 2311-2314.

[85] Lowrie R, Gonas AM, Single-Crystal Elastic Properties of Tungsten from 24° to 1800°C. Journal of applied Physics 1967;38 4505-4509.

IntechOpen